

# SENTINEL-3 OPTICAL PRODUCTS AND ALGORITHM DEFINITION Pixel-by-pixel uncertainty propagation in OLCI clear water branch

Ref.: S3-L2-SD-01-C01-ACR-TN

Version: 2.0

Date: 28/06/2013



Pixel-by-pixel uncertainty propagation in OLCI clear water branch

Ref.: S3-L2-SD-01-C01-ACR-TN

Version: 2.0

Date: 28/06/2013

Page: ii

#### **Signatures**

	Name	Company	Signature
Prepared by	Nicolas Lamquin	ACRI-ST	
	Antoine Mangin	ACRI-ST	
	Constant Mazeran	ACRI-ST	
	Ludovic Bourg	ACRI-ST	
Verified by	Véronique Bruniquel	ACRI-ST	
Approved by	Odile Fanton d'Andon	ACRI-ST	

#### **Distribution list**

Company	То
ESA	Philippe Goryl

#### **Changes Log**

Version	Date	Changes	
2.0	28/06/2013	New version of the document providing the mathematic formulation of radiometric uncertainty propagation, assuming the Level 1 radiometric uncertainty is provided as input, and without considering systematic error model (in either atmospheric or be optical modelling), which are to be added for providing complete product uncertainty.	
1.2	30/09/2010	Updated version including the new LUT generation algorithm and new comparison results	
1.1	16/07/2010	Updated version including the description of error LUT generation	
1.0	03/05/2010	Initial version of the document	



Pixel-by-pixel uncertainty propagation in OLCI clear water branch

Ref.: S3-L2-SD-01-C01-ACR-TN

Version: 2.0

Date: 28/06/2013

Page: iii

#### **Table Of Content**

1	. AB	STRACT	1
2	INT	RODUCTION	2
3		VIEW OF MERIS AND OLCI PROCESSING ABOVE THE OPEN OCEAN	
	3.1	CLEAR WATER ATMOSPHERIC CORRECTION	
	3.2	BIO-OPTICAL INVERSION: CHLOROPHYLL-A, TRANSPARENCY, DIFFUSE ATTENUATION COEFFICIENT	9
4 L		MOTE-SENSING DATA AND CHARACTERIZATION OF INPUT RADIOMETRIC TAINTY	11
5			
3	5.1	ATHEMATICAL UNCERTAINTY COMPUTATION AND VALIDATION	
	5.2	BIO-OPTICAL DATA UNCERTAINTY	
	5.3	Validation	
	5.3		_
	5.3		
6	ME	RIS UNCERTAINTY MAPS OVER THE OPEN OCEAN	
	6.1	METHOD	
	6.2	UNCERTAINTY MAPS	
	6.3	DISCUSSION ON UNCERTAINTY PROPAGATION BY ATMOSPHERIC CORRECTION	36
7	AS	SUMPTIONS AND LIMITATIONS	39
8	RE	FERENCES	40
	NNEX		
Ρ	ROPA	GATION	44



Pixel-by-pixel uncertainty propagation in OLCI clear water branch

Ref.: S3-L2-SD-01-C01-ACR-TN

Version: 2.0

Date: 28/06/2013

Page: iv

#### **List Of Figures**

plane of the Antoine & Morel 1999 scheme. Actual measurement in represented by green dot and radiometric noise distribution in purple9
Figure 2: SPG (left square) and SIO (right square) oligotrophic sites. Background: mean Chlorophyll-a concentration from the 2011 MERIS archive12
Figure 3: TOA radiometric noise estimated at SPG and SIO: terms $\sigma$ 4122, $\sigma$ 412,443, $\sigma$ 412,865 (left, top to bottom) and $\sigma$ 778,560, $\sigma$ 7782, $\sigma$ 778,865 (right, top to bottom)13
Figure 4: Correlation coefficients of TOA radiometric noise $r412,443,\ r412,560,r412,865$ (left, top to bottom) and $r779n442,\ r779,560,r779,865$ (right, top to bottom)15
Figure 5: Comparison between observed (x-axis) and computed (y-axis) uncertainties in marine reflectance; from left to right and top to bottom: $\rho w412$ , $cov\rho w412$ , $\rho w490$ , $cov\rho w412$ , $\rho w560$ and $cov\rho w412$ , $\rho w709$
Figure 6: Comparison between observed (x-axis) and computed (y-axis) uncertainties in marine reflectance; from left to right and top to bottom: $cov\rho w490, \rho w412, \sigma\rho w490, cov\rho w490, \rho w560$ and $cov\rho w490, \rho w709$
Figure 7: Comparison between observed (x-axis) and computed (y-axis) uncertainties in marine reflectance; from left to right and top to bottom: $ov\rho w560, \rho w412 \ cov\rho w560, \rho w490, \sigma \rho w560,$ and $cov\rho w560, \rho w709.$
Figure 8: Comparison between observed (x-axis) and computed (y-axis) uncertainties in marine reflectance; from left to right and top to bottom: $ovpw709, pw412, covpw709, pw490, covpw560, pw709$ and $\sigma pw709$
Figure 9: Degraded comparison between observed (x-axis) and computed (y-axis) uncertainties in marine reflectance at 412 nm (standard deviation) when the TOA covariance terms are not included
Figure 10: Comparison between observed (x-axis) and computed (y-axis) Chl uncertainty, with the complete formulation (left) and when when neglecting the marine reflectance covariance terms (right).
Figure 11: Comparison between observed (x-axis) and computed (y-axis) Kd490 uncertainty24
Figure 12: Validation of the computed $Z_{sd}$ uncertainty (Y axis) against macropixel statistics (X axis)25
Figure 13: Mean correlation coefficient $r\lambda i, \lambda j$ between band $\lambda i$ (colours) and $\lambda j$ (x-axis) as computed on oligotrophic sites
Figure 14: MERIS test scenes over South Pacific Gyre (left) and Hawaii (right): Level 1 composite (top), aerosol optical thickness at 865 nm (middle) and Angstrom coefficient (bottom)28
Figure 15: MERIS marine reflectance (left) and associated uncertainties x10 <sup>3</sup> (right) at bands 412, 490 and 560 (top to bottom) over South Pacific Gyre30
Figure 16: MERIS marine reflectance (left) and associated uncertainties x10 <sup>3</sup> (right) at bands 412, 490 and 560 (top to bottom) over Hawaii31
Figure 17: Comparison between $\rho w490$ uncertainties higher than 2x10 <sup>-4</sup> (top, in red) and {PCD_1_13 or OADB} flags (bottom, in red; background is $\rho w490$ )32
Figure 18: MERIS ocean colour products (left) and associated relative uncertainties (right, in %) at SPG; from top to bottom: chlorophyll ( $mg/m^3$ ), Kd490 ( $m^{-1}$ ) and Secchi depth ( $m$ )34
Figure 19: MERIS ocean colour products (left) and associated relative uncertainties (right, in %) at Hawaii; from top to bottom: chlorophyll (mg/m3), Kd490 (m-1) and Secchi depth (m)35



Pixel-by-pixel uncertainty propagation in OLCI clear water branch

Ref.: S3-L2-SD-01-C01-ACR-TN

Version: 2.0

Date: 28/06/2013

Page: v

Figure 20: Marine reflectance uncertainty at 412 nm (top) and bracketing aerosol model iaer1 (bottom) over Hawaii37
Figure 21: Contributing terms to total uncertainty $var\rho w(412)$ ; terms (c1), (c2), (c3), (c4), (c5) and (c6) refers to equation (32). Scale of variance is multiplied by $10^6$ 38
List Of Tables
Table 1: MERIS reference signal $Lref$ and associated SNR (in reduced resolution) from Delwart 200826



Pixel-by-pixel uncertainty propagation in OLCI clear water branch

Ref.: S3-L2-SD-01-C01-ACR-TN

Version: 2.0

Date: 28/06/2013

Page: 1

#### 1 Abstract

Pixel-by-pixel uncertainty estimate is explicitly required by ESA for the Ocean Colour and Land Imager (OLCI) onboard Sentinel-3. It should be more generally a requirement for any mission, so that remote-sensing data can be used in a relevant manner for scientific studies and downstream applications. We propose here a mathematical framework for the propagation of radiometric noise in marine reflectance and in three bio-optical algorithms: chlorophyll-a, diffuse attenuation coefficient and Secchi depth transparency. The method follows general guidance of BIPM (Bureau International des Poids et Mesures) and GEO (Group on Earth Observations), in particular the QA4EO framework (Quality Assurance Framework for Earth Observation), taking into account spectral variance-covariance matrix of top-of-atmosphere input noise. This study demonstrates it is possible to analytically propagate uncertainties in historical atmospheric correction schemes over clear water and quantifies the impact of spectrally correlated noises. Uncertainty maps on clear waters are computed for the MERIS sensor: absolute uncertainties in marine reflectance at 412 nm, 490 and 560 nm are respectively of about 3.0  $10^{-4}$ , 1.3  $10^{-4}$  and 1.0  $10^{-4}$  (for a 30° solar zenith angle and maritime aerosols), relative uncertainty of chlorophyll is between 3 and 5% and relative uncertainty in Kd and Secchi depth is better than 2%. These numbers have to be added to systematic error model assessed by other means (e.g. theoretical, in-situ) for providing a complete uncertainty estimate. Because uncertainty maps are tributary of the specified sensor noise, here simplified, we emphasise the need to perfectly characterise the spectral structure of instrumental noise after Sentinel-3 launch. In particular the spectral correlation in the Level-1 noise is found to be of major importance for proper uncertainty estimate at Level 2.



Pixel-by-pixel uncertainty propagation in OLCI clear water branch

Ref.: S3-L2-SD-01-C01-ACR-TN

Version: 2.0

Date: 28/06/2013

Page: 2

#### 2 Introduction

Assessment of remote-sensing data uncertainties is one of the main recommendations of the Group on Earth Observations (GEO) within the Quality Assurance Framework for Earth Observation (QA4EO) (Fox, 2010). In this context, uncertainties express numerically how well we measure a quantity from space, hence in which manner we should use it in our own applications for drawing proper conclusions or even for making appropriate decisions. Uncertainty is the opposite of accuracy and is made of the systematic error (bias) and the random error (noise) of the measurement; bias refers to the trueness of the measurement whereas noise refers to its precision.

This paper focus on uncertainties of ocean colour radiometry (OCR) measured data, that is passive remote sensing of Top of Atmosphere ocean surface radiometry from the visible and near-infrared (NIR) regions of the electromagnetic spectrum, and of its derived bio-optical quantities such as e.g. chlorophyll-a concentration, absorption and backscattering of marine components without accounting for the other contributors to the overall uncertainty budget. Altough maps of ocean colour data have constituted for the last decades an important scientific material for climate long-term studies (Behrenfeld et al., 2004, Martinez et al., 2009, Saulquin et al., 2013) as well as for short-term monitoring of the environment, space agencies have never delivered associated uncertainty. In general, an overall quality estimate is made throughout the mission by validating the bio-optical data against punctual concurrent in-situ measurements (e.g Werdell and Bailey 2005 for SeaWiFS and MODIS, Mazeran et al. 2012 for MERIS), a necessary but complex exercise which includes itself other sources of uncertainty (e.g. in-situ measurements errors, heterogeneity in scale between space and ground observation, environmental artifacts like illumination, waves, etc.) and whose geographic and temporal representativeness is limited to that of the ground observation network. The common pixel-by-pixel quality information today provided in OCR data limits to binary flagging (e.g. failure of an algorithm, presence of sun glint, etc.). Some single algorithms may provide an overall uncertainties (e.g. the well-known 30% uncertainties in chlorophyll-a), independently of the actual sensor measurement and without any consideration of upstream algorithms in the data processing chain (e.g. atmospheric correction). The issue has been acknowledged in the OCR community (e.g. Boss and Maritorena 2006) and illustrated (e.g. Hu et al. 2001 for impact of digitization noise). The first successful attempts to derive a systematic per pixel uncertainty at global scale were achieved with the GlobColour dataset (e.g. Fanton d'Andon et al. 2008, Fanton d'Andon et al. 2009, Maritorena et al., 2010) that propagate the uncertainties on marine reflectances to its derived bio-optical quantities. Still we need to go one step further to get the complete end-to-end uncertainty budget from the measured radiometry thoughout the full inversion process. Indeed, potential of OCR data is still strongly limited by lack of systematic uncertainty estimates, required in applications such as operational monitoring (e.g. how well we may derive an environmental indicator, Gohin et al., 2008), multi-sensor merging in view of long-trend building (e.g. which relative confidence to be given to heterogeneous remotesensing sources, Maritorena et al., 2010), or data assimilation (e.g. in biogeochemical global models, Gregg 2008, Triantafyllou et al., 2007). A breakthrough in estimating pixel-based uncertainty of all available geophysical products is now required by the European Space



Pixel-by-pixel uncertainty propagation in OLCI clear water branch

Ref.: S3-L2-SD-01-C01-ACR-TN

Version: 2.0

Date: 28/06/2013

Page: 3

Agency (ESA) for its next generation of OCR sensor, OLCI onboard Sentinel-3 (Nieke *et al.*, 2012, Donlon *et al.*, 2012). This work is a contribution to such a requirement.

Uncertainties in OCR data come from three sources:

- i. Radiometric sensor uncertainties in the visible and NIR channels (at top of atmosphere, TOA) propagating through the processing chain;
- ii. Auxiliary data uncertainties (e.g. meteorological inputs) propagating also through the processing chain;
- iii. Biophysical model uncertainties, both in the forward and backward (numerical inversion) modes (e.g. aerosol modeling in radiative transfer, functional relationship between inherent and apparent optical properties, etc.).

In a schematic input-output process, the two first sources can be grouped together. For the sake of simplicity we will only consider radiometric uncertainties in the following, although the mathematical framework we propose hereafter can deal with both of it. The third source of error is clearly different because it is not related to a given (sensor) measurement. It can be assessed by all sorts of means (theoretically, in laboratory, in-situ...) and does not need remote-sensing data. Model uncertainty tends to decrease thanks to improved knowledge in biology/physics, especially when it is systematic, and will not be considered in this work. In the last years most of the works related to "uncertainties" in ocean colour has focused on this precise contributor (see e.g. Wang et al. 2005, Moore et al. 2009), that we do not cover here. Note that it could be added to the first kind of uncertainties in a global error budget because both are decoupled.

The radiometric uncertainties cover absolute calibration error as well as radiometric noise of the sensor. Strictly speaking, there might be as well spectral calibration error (i.e. uncertainties on the exact wavelengths at which the light is measured), but this can be transferred in term of radiometric uncertainties. Major efforts are developed by space agencies to ensure the best sensor calibration at TOA level, e.g. about 2% accuracy for MERIS (Bourg and Delwart, 2013). Eventually, a vicarious calibration helps to remove the residual TOA biases, thanks to ground-trust measurements (Franz et al., 2007, Lerebourg et al., 2011). For this reason, we will not consider TOA bias in this study.

This work thus focuses on the propagation of radiometric noise at TOA level in the OCR processing chain, in order to estimate uncertainties of bio-optical data, apart from systematic errors assumed to be already corrected for. Having in mind the preparation of the future OLCI sensor, we base this demonstration on the past MERIS sensor, whose design is similar and algorithms of interest are identical. In order to put this work in a broader perspective we retain the core steps of the processing, namely the atmospheric correction and the bio-optical inversion over the open ocean, outside the sun glint contamination region, hence where algorithms are considered as mature enough. Practically we consider a full "Case 1" chain, made of:

The clear water atmospheric from Antoine and Morel, 1999;



Pixel-by-pixel uncertainty propagation in OLCI clear water branch

Ref.: S3-L2-SD-01-C01-ACR-TN

Version: 2.0

Date: 28/06/2013

Page: 4

The chlorophyll-a index and Kd at 490 nm from Morel *et al.*, 2007, and the Secchi depth of Doron *et al.*, 2007.

Importantly, this domain of application does not come from methodological constraints - other processors designed for coastal waters could be included, as discussed further - and is just enough to demonstrate our approach on well-known historical algorithms operationally used by space agencies for past, current, and future missions.

The error propagation we propose here is totally analytical (no simulation, as e.g. in Wang et al., 2005) and follows the mathematical formalism recommended in the QA4EO group (Fox, 2010), after the "Guide to the expression of uncertainty in measurement" by the Joint Committee for Guides in Metrology (JCGM, 2008). It is also different than the uncertainties propagation in an analytical ocean color algorithm studied by Lee et al. 2010 because it includes the crucial role of error correlation between independent variables. To summarise quickly this method, let us consider a scalar function f of a N-dimensional random variable  $x = (x_1, x_2, \cdots, x_N)$ , this latter being the sum of a target (true) term  $\overline{x}$  and random error  $\varepsilon$ :

$$x = \overline{x} + \varepsilon \tag{1}$$

We assume that errors follow a multivariate normal-law centered on a systematic bias  $\boldsymbol{b}$  and with known noise, characterised by the symmetric variance-covariance matrix  $\boldsymbol{c}$ :

$$\boldsymbol{\varepsilon} \sim \mathcal{N}(\boldsymbol{b}, \boldsymbol{C}), \quad \boldsymbol{C} = \begin{pmatrix} \sigma_1^2 & \sigma_{1,2} & \cdots & \sigma_{1,N} \\ \sigma_{1,2} & \sigma_2^2 & \cdots & \sigma_{2,N} \\ \vdots & \vdots & \ddots & \vdots \\ \sigma_{1,N} & \sigma_{2,N} & \cdots & \sigma_N^2 \end{pmatrix}$$
(2)

where term  $\sigma_{i,j}$  represents the covariance of inputs  $(x_i, x_j)$ ; in this case we recall that the probability distribution function (PDF) of  $\varepsilon$  is equal to

$$p(\varepsilon) = \frac{1}{\sqrt{(2\pi)^N |\mathcal{C}|}} e^{-\frac{1}{2}(\varepsilon - b) \cdot \mathcal{C}^{-1}(\varepsilon - b)}$$
(3)

If the function is differentiable, a first order Taylor expansion gives

$$f(x) \approx f(\overline{x}) + \nabla f(\overline{x}) \cdot \varepsilon$$
 (4)

The output variance var(f) due to the input uncertainty  $\varepsilon$  is obtained by computing the second moment of f(x), taking into account the PDF:

$$var(f) = \nabla f(\overline{x}) \cdot C \nabla f(\overline{x}) \tag{5}$$

For instance in the case of a bio-optical algorithm based on two marine remote-sensing reflectances  $(R_{rs1}, R_{rs2}) \rightarrow f(R_{rs1}, R_{rs2})$ , one has



Pixel-by-pixel uncertainty propagation in OLCI clear water branch

Ref.: S3-L2-SD-01-C01-ACR-TN

Version: 2.0

Date: 28/06/2013

Page: 5

$$\sigma_f^2 = \left(\frac{\partial f}{\partial R_{rs1}}, \frac{\partial f}{\partial R_{rs2}}\right) \begin{pmatrix} \sigma_{R_{rs1}}^2 & \sigma_{R_{rs1}, R_{rs2}} \\ \sigma_{R_{rs1}, R_{rs2}} & \sigma_{R_{rs2}}^2 \end{pmatrix} \begin{pmatrix} \frac{\partial f}{\partial R_{rs1}} \\ \frac{\partial f}{\partial R_{rs2}} \end{pmatrix}$$
(6)

which, importantly, depends on the variance-covariance matrix of the marine reflectances. This means that, at several stages of the OCR processing, it may be necessary to estimate the covariance between two simultaneously computed quantities. In that aim, the same mathematical formalism can be extended to a vector-valued function  $\mathbf{f} = (f_1, f_2, \cdots, f_M)$ , whose uncertainties variance-covariance matrix  $\mathbf{cov}(\mathbf{f})$  is now given by the following matrix products (the prime symbol represent the transpose):

$$\mathbf{cov}(\mathbf{f}) = \nabla f(\overline{x})' \, C \, \nabla f(\overline{x}) \tag{7}$$

Consider for example two functions  $f_1$ ,  $f_2$  of partially common inputs:  $(x_1, x_3, x_4) \rightarrow f_1(x_1, x_3, x_4)$  and  $(x_2, x_3, x_4) \rightarrow f_2(x_2, x_3, x_4)$ , their covariance simplifies to computation of

$$cov(f_1, f_2) = \left(\frac{\partial f_1}{\partial x_1}, \frac{\partial f_1}{\partial x_3}, \frac{\partial f_1}{\partial x_4}\right) \begin{pmatrix} \sigma_{1,2} & \sigma_{1,3} & \sigma_{1,4} \\ \sigma_{2,3} & \sigma_3^2 & \sigma_{3,4} \\ \sigma_{2,4} & \sigma_{3,4} & \sigma_4^2 \end{pmatrix} \begin{pmatrix} \frac{\partial f_2}{\partial x_2} \\ \frac{\partial f_2}{\partial x_3} \\ \frac{\partial f_2}{\partial x_4} \end{pmatrix}$$
(8)

In this paper we will particularly prove that such algebra is rigorously applicable to pixel-by-pixel standard atmospheric correction schemes (here Antoine and Morel, 1999, similar in the principle as Gordon and Wang, 1994) while they are generally considered as complex and not suitable for such an exercise. Interestingly, this formalism can deal with any other PDFs characterizing the input noise  $\varepsilon$ , as well as pixel-dependent noise (e.g. function of the radiometry amplitude). Note also that the very same computations of var(f) and  $cov(f_i, f_j)$  remain perfectly right in presence of a bias  $\boldsymbol{b}$ , a situation we however do not consider in the present study.

Through this methodology, the goal of this work is twofold:

- i. First demonstrate the absolute need to take into account the exact structure of the input uncertainties (typically the variance-covariance matrix in case of multivariate normal-law distribution) and to mathematically understand their combined effect on the output uncertainty. This is here illustrated at both the atmospheric correction and bio-optical inversion levels. For multispectral algorithm this essentially means error cancellation thanks to spectral correlation in the noise.
- ii. Second, generate uncertainty maps at global scale (open ocean) of water-leaving reflectance, chlorophyll-a, diffuse attenuation coefficient and transparency. These



Pixel-by-pixel uncertainty propagation in OLCI clear water branch

Ref.: S3-L2-SD-01-C01-ACR-TN

Version: 2.0

Date: 28/06/2013

Page: 6

maps are intrinsic to the sensor and the processing chain (here MERIS in preparation of OLCI), and totally independent of in-situ data or other sensors (see *e.g.* Mélin, 2010 for uncertainties derived by comparison between two sensors). We remind that these uncertainties do not include error model, which could be added.

This paper is arranged as follows. Section 2 introduces the physics and notations of the study by reviewing the OLCI atmospheric correction and three bio-optical algorithms: chlorophylla, diffuse attenuation coefficient and Secchi depth transparency. Section 3 describes the remote-sensing data used in this study (MERIS) and characterises the input noise at top of atmosphere. Section 4 details the mathematical uncertainty computation in the full chain (atmospheric correction and bio-optical inversion) and its validation; we here demonstrate the effect of marine reflectance spectral correlation errors in bio-optical algorithms. Uncertainty maps are presented in section 5 with a discussion on error propagation.



Pixel-by-pixel uncertainty propagation in OLCI clear water branch

Ref.: S3-L2-SD-01-C01-ACR-TN

Version: 2.0

Date: 28/06/2013

Page: 7

# 3 Review of MERIS and OLCI processing above the open ocean

#### 3.1 Clear water atmospheric correction

Retrieval of the sea surface radiometry from space needs to correct the top-of-atmosphere acquisition from absorption and scattering of the atmosphere, which represent around 90% of the total signal over clear waters. Although other effects such as sun specular reflection, white-caps, haze, are also important issues faced in ocean colour, we do not consider them in this paper in order to focus on the core of the processing chain; their contribution can be either avoided by instrumental configuration (e.g. depointing mechanism for OLCI, Infrared bands for cloud detection) or be already corrected by upstream processings (e.g. Cox and Munk 1954 for sun glitter correction) providing their own error budget. Considering the wavelength of interest (from 400 nm to 900 nm), atmospheric effects comprise absorption by gas (oxygen, water vapour and ozone), Rayleigh and aerosols scattering and their multiple scattering. Gaseous absorption is generally handled with great confidence, as well as the pure Rayleigh scattering. The main challenge of atmospheric correction is to retrieve the unknown amount and type of aerosols, variable in space and time.

We adopt here the formalism of Antoine and Morel 1999 used in the MERIS and OLCI ground segment chains noting that our mathematical framework for uncertainties propagation would be totally transferable to analogous schemes of other missions (e.g. MODIS with Gordon and Wang 1994). In this approach, the whole path reflectance  $\rho_{path}$  is considered, taking into account the Rayleigh and aerosol reflectance as well as the multiple-scattering contribution. The reflectance is pre-computed by a radiative transfer code (Zagolski, 2010) for a set of illumination and viewing geometries, wind modulus (not mentioned hereafter for the sake of legibility), and aerosol assemblages and optical thicknesses. Practically, the ratio of the total path reflectance by the pure Rayleigh reflectance,  $\zeta$ , is tabulated for each aerosol assemblage ia and wavelength  $\lambda$  as a second degree polynomial  $\mathcal{P}_{\lambda}^{ia}$  of the aerosol optical thickness  $\tau_{\lambda}$ :

$$\mathcal{P}_{\lambda}^{ia} \colon \tau_a(\lambda) \to \frac{\rho_{path}}{\rho_R}(\lambda) \stackrel{\text{def}}{=} \zeta_{\lambda}$$
 (9)

This ratio used in the MERIS ground segment in view of reducing the effect of changes in barometric pressure (Antoine and Morel, 1998). Also, Mie theory provides the spectral dependence of aerosol optical thickness,  $c_{\lambda}^{ia}$ , starting from its value at 865 nm, through tabulated non-linear relationships:

$$\tau_a(\lambda) = \tau_a(865) * c_{\lambda}^{ia}(\tau_a(865))$$
 (10)

Eventually, total atmospheric transmittance t (downward and upward, diffuse + direct) is stored in look-up tables  $\mathcal{T}^{ia}_{\lambda}$  as a function of optical thickness for the same set of conditions as the reflectance (in particular model and wavelength):

$$\mathcal{T}_{\lambda}^{ia} \colon \tau_{a}(\lambda) \to t(\lambda)$$
 (11)



Pixel-by-pixel uncertainty propagation in OLCI clear water branch

Ref.: S3-L2-SD-01-C01-ACR-TN

Version: 2.0

Date: 28/06/2013

Page: 8

These three relationships characterise entirely the atmospheric reflectance and transmittances at any wavelength. From two measurements of  $\rho_{path}$  in the NIR (at 779 and 865 nm), these relationships allow, schematically, to retrieve the two unknown optical thickness  $\tau_{865}$  and aerosol model ia. More precisely, two aerosol models (ia1,ia2) are selected which best bracket the signal at 779 nm, and a mixing ratio is defined to weight their relative contribution (see Figure 1 and section 5.1 hereafter for detailed equations). Information on  $\rho_{path}$  in the NIR is given by the sensor acquisition, either directly by assumption of the black water assumption or after a pre-correction for residual turbid signal (e.g. Moore and Lavender, 2011 for MERIS).

Hence, starting from a TOA reflectance  $\rho_{gc}$  corrected for gaseous absorption, glint, and white-caps, the marine reflectance at sea level at any wavelength  $\lambda_{VIS}$  in the visible is computed by the basic equation

$$\rho_{w}(\lambda_{VIS}) = \frac{\rho_{gc}(\lambda_{VIS}) - \rho_{path}(\lambda_{VIS}) * C_{\Delta P} + (\lambda_{VIS})}{t(\lambda_{VIS})}$$
(12)

Where  $\rho_{path}(\lambda_{VIS})$  and  $t(\lambda_{VIS})$  are the path reflectance and total transmittance deduced in the visible bands by stored computations  $\mathcal{P}^{ia}_{\lambda}$  and  $\mathcal{T}^{ia}_{\lambda}$  and from knowledge of aerosol optical thickness, aerosol models and mixing ratio. The corrective term  $\mathcal{C}_{\Delta P^+}$  accounts for the actual pressure P of the acquisition because tabulated reflectances are only computed at standard pressure ( $P_{std}$  = 1013 hPa):

$$C_{\Delta P} + (\lambda_{VIS}) = 1 + \Delta P \frac{\tau_R(\lambda_{VIS})}{\tau_R(\lambda_{VIS}) + \tau_a(\lambda_{VIS})}, \text{ with } \Delta P = \frac{P - P_{std}}{P_{std}}$$
(13)

Where  $\tau_R$  is the Rayleigh optical thickness. Note that a reverse correction  $\mathcal{C}_{\Delta P^-}$  must also be applied preliminarily in the NIR in order to transfer  $\rho_{path}(\lambda_{NIR})$  at  $P_{std}$ , before using the stored polynomial  $\mathcal{P}^{ia}_{\lambda}$ ; however at this prior stage the unknown aerosol optical is given a unique value, 0.1, for the sake of simplicity:

$$\rho_{path}(\lambda_{NIR}) = C_{\Delta P^{-}}(\lambda_{NIR})\rho_{gc}(\lambda_{NIR}) \quad \text{with } C_{\Delta P^{-}}(\lambda_{NIR}) = 1 - \Delta P \frac{\tau_{R}(\lambda_{NIR})}{\tau_{R}(\lambda_{NIR}) + 0.1}$$
(14)

Uncertainty propagation of  $\rho_{gc}$  (top of atmosphere) to  $\rho_w$  (sea level) thus takes place at two levels:

- i. First, uncertainty in  $\rho_{gc}(\lambda_{NIR})$  affects the aerosol model selection, mixing ratio, optical thickness hence  $\rho_{path}(\lambda_{VIS})$ ,  $C_{\Delta P}+(\lambda_{VIS})$  and  $t(\lambda_{VIS})$
- ii. Then uncertainty in  $\rho_{gc}(\lambda_{VIS})$  is directly integrated into  $\rho_w(\lambda_{VIS})$

It is empirically well-known that noise in the NIR can strongly impact the marine signal in the visible. As depicted on Figure 1, effect depends on the distribution on the input uncertainties: clearly correlated errors at 779 and 865 nm will minimize the impact on aerosol selection.



Pixel-by-pixel uncertainty propagation in OLCI clear water branch

Ref.: S3-L2-SD-01-C01-ACR-TN

Version: 2.0

Date: 28/06/2013

Page: 9

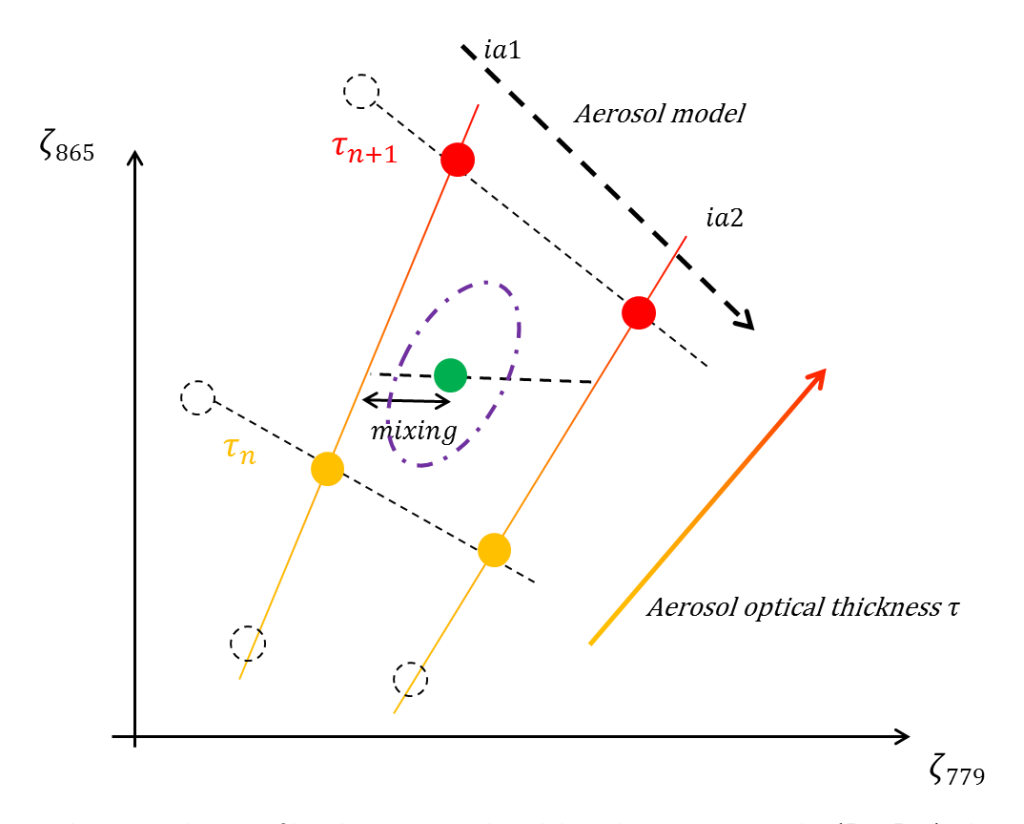


Figure 1: Schematic selection of bracketing aerosol models and mixing ratio in the  $(\zeta_{779}, \zeta_{865})$  plane of the Antoine & Morel 1999 scheme. Actual measurement in represented by green dot and radiometric noise distribution in purple

# 3.2 Bio-optical inversion: chlorophyll-a, transparency, diffuse attenuation coefficient

Remote sensing reflectances  $\rho_w$  at several wavelengths in the visible/NIR are the main inputs to further compute marine constituents concentrations or inherent optical properties; this possibly needs to consider fully normalised reflectance  $\rho_{wN}$  after correction for bidirectional effects (Morel  $et\ al.$ , 2002), a step we do not explicit here because it only implies multiplicative factors not amplifying the radiometric noise.

We here review three historical bio-optical algorithms, planned to be implemented in the the clear water branc of OLCI Level 2 processing.

Chlorophyll-a concentration (Morel et al., 2007) - The OC4Me algorithm computes the Chlorophyll-a concentration (in  $mg/m^3$ ) using a polynomial relationship on the blue-to-green band ratio in irradiance reflectances R:

$$\log_{10} \text{Chl} = \sum_{i=0}^{N} A_i \left( \log_{10} \frac{R_1}{R_2} \right)^i$$
 (15)

The exact choice on reflectance corresponds to the maximizing ratio between 412/560, 443/560 and 490/560, but once the best channels are identified, this is a two-band



Pixel-by-pixel uncertainty propagation in OLCI clear water branch

Ref.: S3-L2-SD-01-C01-ACR-TN

Version: 2.0

Date: 28/06/2013

Page: 10

algorithm. This band ratio is based on the Morel and Maritorena, 2001 reflectance model. Conversion from water-leaving reflectance (OLCI primary output) to irradiance reflectance is defined in Antoine and Fanton d'Andon, 2012.

Diffuse attenuation coefficient at 490 nm (Morel et al., 2007) – In a similar way the  $K_d(490)$  product (in m<sup>-1</sup>) is computed by the OK2-560 algorithm, using a ratio between irradiance reflectances at 490 nm and 560 nm:

$$K_d(490) = K_w(490) + 10^{\sum_{i=0}^{N} B_i \left(\log_{10} \frac{R_{490}}{R_{560}}\right)^i}$$
 (16)

Secchi disk depth transparency – The Secchi disk depth transparency algorithm considered here is the empirical alternative of Doron *et al.*, 2007. It uses a ratio between irradiance reflectances just below the surface  $R(0^-)$  at 490 nm and at 560 nm:

$$Z_{sd} = \gamma \cdot \left( a \frac{R^{-}(490)}{R^{-}(560)} + b \right) \tag{17}$$

Where a and b are constants,  $R^-(\lambda)=\frac{\rho_{wN}(\lambda)}{A_\lambda+B_\lambda\rho_{wN}(\lambda)}$  with  $A_\lambda$  and  $B_\lambda$  constants at a given wavelength, and  $\gamma=\alpha_{490}\gamma(490)+\alpha_{560}\gamma(560)$  with  $\gamma(\lambda)=\ln\frac{R_{sd}-R^-(\lambda)}{C_{min}\cdot R^-(\lambda)}$ ,  $C_{min}$  being the minimum apparent contrast perceivable by the human eye and  $R_{sd}$  the Secchi disk reflectance.

An important property of these algorithms is to be analytical, what will naturally help for derivative computation and rigorous error propagation.



Pixel-by-pixel uncertainty propagation in OLCI clear water branch

Ref.: S3-L2-SD-01-C01-ACR-TN

Version: 2.0

Date: 28/06/2013

Page: 11

# 4 Remote-sensing data and characterization of input radiometric uncertainty

OLCI sensor planned for launch in 2014 has been designed upon a close heritage to MERIS, in term of main spectral bands, radiometric performance and imaging design (Donlon *et al.*, 2012, Nieke *et al.*, 2012). The processing chain at Level 2 (i.e. from calibrated and geolocated TOA radiances to biogeophysical quantities) shares also many commonality, in particular regarding the clear water branch. For this reason we develop and validate our uncertainty propagation on available MERIS data, from the 3<sup>rd</sup> ESA reprocessing (MERIS QWG, 2011). Reduced resolution pixels (RR, about 1.2km ground resolution) are enough to illustrate the approach and consistent with the future OLCI binned mode over the open ocean. We remind that MERIS 3<sup>rd</sup> reprocessing TOA reflectances above the ocean are vicariously adjusted, that is corrected as much as possible for systematic biases in the visible and NIR bands (Lerebourg *et al.*, 2011). This also justifies our work assumption to only consider random noise.

Little is known on MERIS pixel-by-pixel radiometric noise – and more generally for any other OCR sensor - because of the difficulty to model photonic, detector and electronic noises. Classically the noise equivalent radiance difference ( $NE\Delta L$ ) at a given wavelength  $\lambda$  expresses the expected total noise at TOA and is related to the signal to noise ratio (SNR), specified before launch for a reference radiance  $L_{ref}$ :

$$SNR(\lambda) = \frac{L_{ref}(\lambda)}{NE\Delta L(\lambda)}$$
 (18)

Because such noise is generally assumed to vary as the square root of the radiance, it can be deduced for an actual pixel of radiance L by

$$\sigma(\lambda) = NE\Delta L(\lambda) \frac{\sqrt{L(\lambda)}}{\sqrt{L_{ref}}(\lambda)}$$
 (19)

The SNR specification is however limited because first it may not rigorously quantify the actual  $NE\Delta L$  (or equivalently the SNR) and second it does not inform on possible spectral covariance in the radiometric noise. For MERIS, two post-launch estimates of SNR were published to our knowledge: a characterisation with the solar diffuser in RR mode during the commissioning phase in 2002 (see Delwart, 2008) and a more recent computation of SNR on homogenous oceanic targets by Hu et~al., 2012, both in FR and RR mode. Practical interest of the latter approach is to be manageable with data of the sensor only, yet it needs a careful filtering. We here follow a similar approach, in view of computing all covariance terms  $\sigma_{\lambda i,\lambda j}$  between radiances  $L(\lambda_i)$  and  $L(\lambda_i)$ , never quantified so far.

We conduct the uncertainty characterization on Level 1 data over spatially homogeneous oceanic zones, i.e. the South Pacific Gyre (SPG, 27.0° S, 134° W) and the South Indian Ocean (SIO, 20.0° S, 80.0° E), see Figure 2. In such oligotrophic regions the marine reflectance in the



Pixel-by-pixel uncertainty propagation in OLCI clear water branch

Ref.: S3-L2-SD-01-C01-ACR-TN

Version: 2.0

Date: 28/06/2013

Page: 12

NIR is negligible, so that we will be able to restrict the atmospheric correction to the clear water branch. The local pixel variability over these areas provides us with information on the radiometric noise, but also non-instrumental artefacts potentially impacting the ocean colour products (e.g. foams).

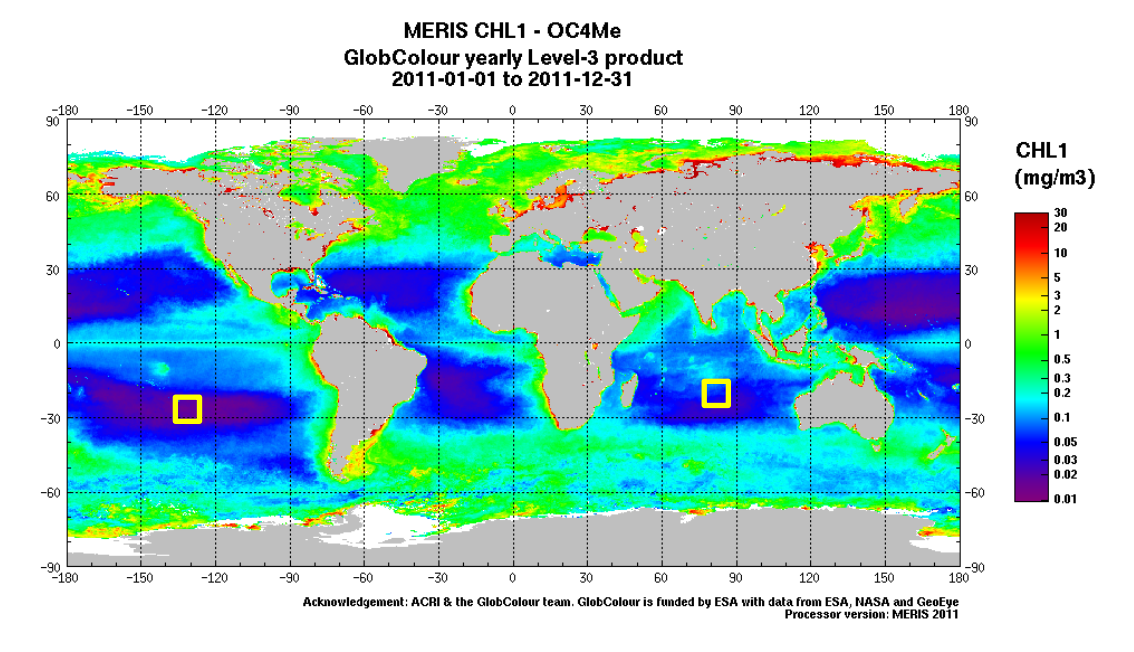


Figure 2: SPG (left square) and SIO (right square) oligotrophic sites. Background: mean Chlorophyll-a concentration from the 2011 MERIS archive.

From the whole MERIS data archive between 2003 and 2009 (about 4600 Reduced Resolution images) we have selected data with the best observation conditions (no clouds, no glint), following strictly the selection of Lerebourg et~al., 2011 for the determination of the MERIS vicarious adjustment gains in the NIR. Finally, more than 3000 windows of 5x5 pixels are gathered. On each window we compute the variance-covariance matrix  $\sigma_{\lambda i,\lambda j}$  of the TOA reflectances ( $\rho_{gc}$ ). Importantly, we removed the pixels flagged as duplicated in the MERIS files (due to grid resampling, in particular near the edge of the swath) in order not to artificially decrease the variance and covariance.

Let us emphasize that this approach is not as evolved as e.g. Hu *et al.*, 2012, because our goal is not to perfectly estimate SNR in absolute value, but to validate uncertainty propagation. Hence the most important aspect of our methodology is to apply the same metric as input (TOA reflectance) and output (ocean colour products at sea level), the metric being here considered as spatial variance for the sake of simplicity.

Examples of TOA uncertainty at some wavelengths are shown in Figure 3 as a function of the TOA signal itself. We observe a large dispersion which stresses the difficulty of modeling this noise as a function of the signal, at least with such a simple approach. Amplitudes are low  $(10^{-7} - 10^{-8})$  but we shall see that they perfectly explain the uncertainties on the water reflectances and derived ocean colour products.



Pixel-by-pixel uncertainty propagation in OLCI clear water branch

Ref.: S3-L2-SD-01-C01-ACR-TN

Version: 2.0

Date: 28/06/2013

Page: 13

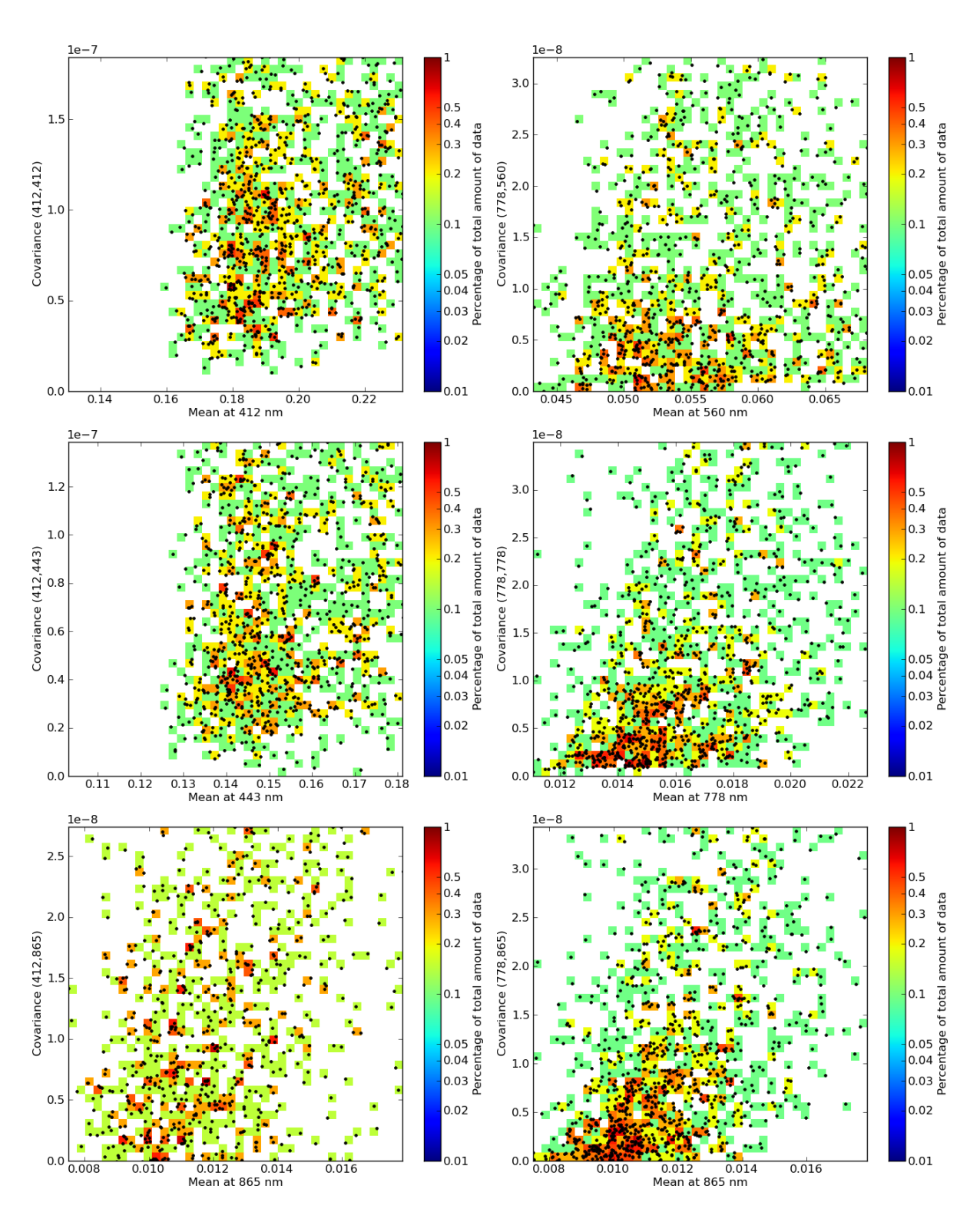


Figure 3: TOA radiometric noise estimated at SPG and SIO: terms  $\sigma_{412}^2$ ,  $\sigma_{412,443}$ ,  $\sigma_{412,865}$  (left, top to bottom) and  $\sigma_{778,560}$ ,  $\sigma_{778,865}^2$ ,  $\sigma_{778,865}$  (right, top to bottom)



Pixel-by-pixel uncertainty propagation in OLCI clear water branch

Ref.: S3-L2-SD-01-C01-ACR-TN

Version: 2.0

Date: 28/06/2013

Page: 14

The covariance terms  $\sigma_{\lambda i,\lambda j}$  correspond to the spectral correlations of TOA noise which is integrated within our mathematical framework. The correlation coefficient is defined by:

$$r_{\lambda i,\lambda j} = \frac{\sigma_{\lambda i,\lambda j}}{\sigma_{\lambda i} \sigma_{\lambda j}} \tag{20}$$

On Figure 4 we observe that this correlation is close to unity when two bands are spectrally close (e.g 779 and 865 nm) and weaker when they become more separated. To our knowledge it is the first time that these correlations have been identified on an ocean colour sensor (here MERIS). The fact that noise at 779 and 865 nm are strongly correlated directly impacts the atmospheric corrections and consequently partly compensates noise propagation. Results in the next sections show that this compensation is significant and that there is a real need to properly characterize the covariance terms  $\sigma_{\lambda i,\lambda j}$  at sensor level.



Pixel-by-pixel uncertainty propagation in OLCI clear water branch

Ref.: S3-L2-SD-01-C01-ACR-TN

Version: 2.0

Date: 28/06/2013

Page: 15

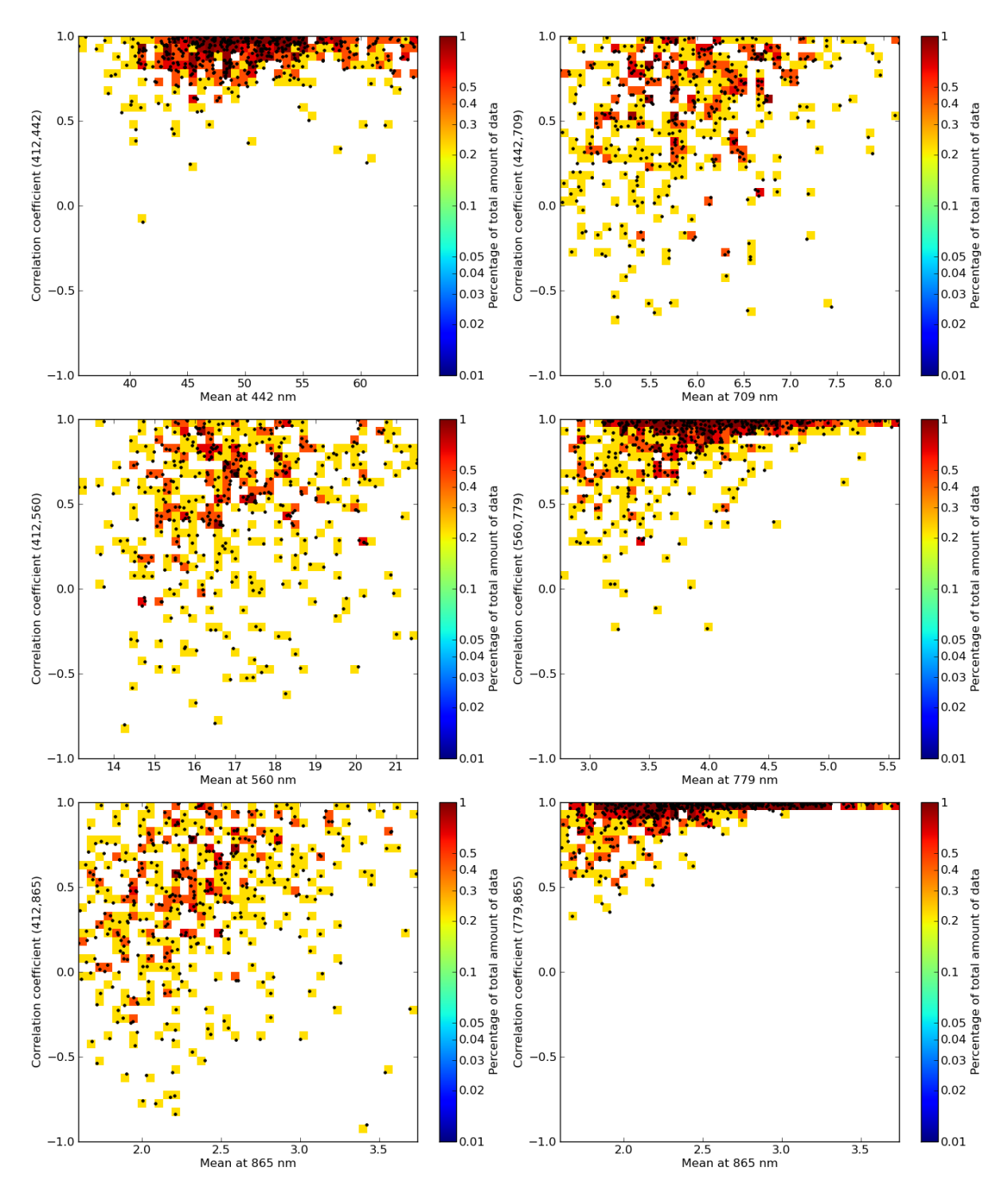


Figure 4: Correlation coefficients of TOA radiometric noise  $r_{412,443}$ ,  $r_{412,560}$ ,  $r_{412,865}$  (left, top to bottom) and  $r_{779,442}$ ,  $r_{779,560}$ ,  $r_{779,865}$  (right, top to bottom)



Pixel-by-pixel uncertainty propagation in OLCI clear water branch

Ref.: S3-L2-SD-01-C01-ACR-TN

Version: 2.0

Date: 28/06/2013

Page: 16

#### 5 Mathematical uncertainty computation and validation

#### 5.1 Marine reflectance uncertainty

We now derive the analytical expression of marine reflectances uncertainties. From equation (12), we can rewrite the marine reflectance as a function of three variables, linked to TOA signal at  $\lambda$ , 779 and 865 nm:

$$\rho_{w}(\lambda) = \rho_{w}(\lambda, x, y, z) = \frac{x - \zeta_{\lambda}(y, z) * C_{\Delta P} + (\lambda, y, z)}{t_{\lambda}(y, z)} \rho_{R}(\lambda)$$
 (21)

With 
$$x = \frac{\rho_{gc}}{\rho_R}(\lambda)$$
,  $y = \zeta_{779} * C_{\Delta P}$ -(779),  $z = \zeta_{865} * C_{\Delta P}$ -(865)

Such a formulation comes from the fact that the scheme is written in term of the  $\zeta$  ratio, cf. equation (9). We recall that  $C_{\Delta P^+}$  is also a function of y and z (through the aerosol optical thickness), unlike  $C_{\Delta P^-}$ . In the scheme  $\zeta_\lambda$  for  $\lambda$  in the visible is a mixing between the values extrapolated from the NIR by two bracketing aerosol models, indexed by (ia1, ia2). Band at 865 nm (related to z variable) is used to determine the aerosol optical thickness and band at 779 nm (related to y variable) is used to determine the best aerosol models. The mixing writes:

$$\zeta_{\lambda}(y,z) = \left(\zeta_{\lambda}^{ia2}(z) - \zeta_{\lambda}^{ia1}(z)\right) mix(y,z) + \zeta_{\lambda}^{ia1}(z)$$

$$\ln t_{\lambda}(y,z) = \left(\ln t_{\lambda}^{ia2}(z) - \ln t_{\lambda}^{ia1}(z)\right) mix(y,z) + \ln t_{\lambda}^{ia1}(z)$$
(22)

Where  $\zeta_{\lambda}^{ia}(z)$  and  $t_{\lambda}^{ia}$  are respectively the computed  $\frac{\rho_{path}}{\rho_R}$  ratio and total transmittance for aerosol model ia, which both only depends on  $\zeta_{865}$ , hence z. The mixing ratio is defined at band 779 nm by

$$mix(y,z) = \frac{y - \zeta_{779}^{ia1}(z)}{\zeta_{779}^{ia2}(z) - \zeta_{779}^{ia1}(z)}$$
(24)

Applying the general mathematical formalism of uncertainty propagation yields to

$$var(\rho_{w}(\lambda)) = \left(\frac{\partial \rho_{w}(\lambda)}{\partial x}, \frac{\partial \rho_{w}(\lambda)}{\partial y}, \frac{\partial \rho_{w}(\lambda)}{\partial z}\right) C_{\lambda} \begin{pmatrix} \frac{\partial \rho_{w}(\lambda)}{\partial x} \\ \frac{\partial \rho_{w}(\lambda)}{\partial y} \\ \frac{\partial \rho_{w}(\lambda)}{\partial z} \end{pmatrix}$$
(25)

Where the variance-covariance matrix  $C_{\lambda}$  is defined by



Pixel-by-pixel uncertainty propagation in **OLCI clear water branch** 

Ref.: S3-L2-SD-01-C01-ACR-TN

(31)

Version: 2.0

Date: 28/06/2013

Page: 17

$$C_{\lambda} = \begin{pmatrix} \frac{\sigma_{\lambda}^{2}}{\rho_{R}^{2}(\lambda)} & \frac{\sigma_{\lambda,779} * C_{\Delta P^{-}}(779)}{\rho_{R}(\lambda)\rho_{R}(779)} & \frac{\sigma_{\lambda,865} * C_{\Delta P^{-}}(865)}{\rho_{R}(\lambda)\rho_{R}(865)} \\ \frac{\sigma_{\lambda,779} * C_{\Delta P^{-}}(779)}{\rho_{R}(\lambda)\rho_{R}(779)} & \frac{\sigma_{779}^{2} * C_{\Delta P^{-}}^{2}(779)}{\rho_{R}^{2}(779)} & \frac{\sigma_{779,865} * C_{\Delta P^{-}}(779) * C_{\Delta P^{-}}(865)}{\rho_{R}(779)\rho_{R}(865)} \\ \frac{\sigma_{\lambda,865} * C_{\Delta P^{-}}(865)}{\rho_{R}(\lambda)\rho_{R}(865)} & \frac{\sigma_{779,865} * C_{\Delta P^{-}}(779) * C_{\Delta P^{-}}(865)}{\rho_{R}(779)\rho_{R}(865)} & \frac{\sigma_{865}^{2} * C_{\Delta P^{-}}^{2}(865)}{\rho_{R}^{2}(865)} \end{pmatrix}$$

$$(26)$$

Here the  $\sigma_{\lambda i,\lambda j}$  terms are the input variances and covariances of the TOA glint-corrected reflectances  $\rho_{ac}(\lambda)$ .

In the same manner, the uncertainty covariance  $cov\left(
ho_w(\lambda_i),
ho_w(\lambda_j)\right)$  is given by

$$cov\left(\rho_{w}(\lambda_{i}), \rho_{w}(\lambda_{j})\right) = \left(\frac{\partial \rho_{w}(\lambda_{i})}{\partial x i}, \frac{\partial \rho_{w}(\lambda_{i})}{\partial y}, \frac{\partial \rho_{w}(\lambda_{i})}{\partial z}\right) C_{\lambda_{i}, \lambda_{j}} \begin{pmatrix} \frac{\partial \rho_{w}(\lambda_{j})}{\partial x j} \\ \frac{\partial \rho_{w}(\lambda_{j})}{\partial y} \\ \frac{\partial \rho_{w}(\lambda_{j})}{\partial z} \end{pmatrix}$$
(27)

Where we note  $x_i = \frac{\rho_{gc}}{\rho_R}(\lambda_i)$  and now  $C_{\lambda_i,\lambda_j}$  is a <u>nonsymmetric</u> matrix

Where we note 
$$x_i = \frac{\rho_{gc}}{\rho_R}(\lambda_i)$$
 and now  $C_{\lambda_i,\lambda_j}$  is a nonsymmetric matrix 
$$C_{\lambda_i,\lambda_j} = \begin{pmatrix} \frac{\sigma_{\lambda i,\lambda j}}{\rho_R(\lambda_i)\rho_R(\lambda_j)} & \frac{\sigma_{\lambda i,779} * C_{\Delta P^-}(779)}{\rho_R(\lambda_i)\rho_R(779)} & \frac{\sigma_{\lambda i,865} * C_{\Delta P^-}(865)}{\rho_R(\lambda_i)\rho_R(865)} \\ \frac{\sigma_{\lambda_j,779} * C_{\Delta P^-}(779)}{\rho_R(\lambda_j)\rho_R(779)} & \frac{\sigma_{779} * C_{\Delta P^-}^2(779)}{\rho_R^2(779)} & \frac{\sigma_{779,865} * C_{\Delta P^-}(779) * C_{\Delta P^-}(865)}{\rho_R(779)\rho_R(865)} \\ \frac{\sigma_{\lambda_j,865} * C_{\Delta P^-}(865)}{\rho_R(\lambda_j)\rho_R(865)} & \frac{\sigma_{779,865} * C_{\Delta P^-}(779) * C_{\Delta P^-}(865)}{\rho_R(779)\rho_R(865)} & \frac{\sigma_{865}^2 * C_{\Delta P^-}^2(865)}{\rho_R^2(865)} \end{pmatrix}$$

Uncertainty estimates hence come down to computation of partial derivatives of  $\rho_w(\lambda, x, y, z)$ :

$$\frac{\partial \rho_{w}(\lambda)}{\partial x} = \frac{\rho_{R}(\lambda)}{t_{\lambda}(y,z)} \tag{29}$$

$$\frac{\partial \rho_{w}(\lambda)}{\partial y} = -\frac{\frac{\partial \left(\zeta_{\lambda}(y,z)C_{\Delta P}+(\lambda,y,z)\right)}{\partial y}\rho_{R}(\lambda) + \rho_{w}(\lambda)\frac{\partial t_{\lambda}(y,z)}{\partial y}}{t_{\lambda}(y,z)}$$

$$\frac{\partial \rho_{w}(\lambda)}{\partial z} = -\frac{\frac{\partial \left(\zeta_{\lambda}(y,z)C_{\Delta P}+(\lambda,y,z)\right)}{\partial z}\rho_{R}(\lambda) + \rho_{w}(\lambda)\frac{\partial t_{\lambda}(y,z)}{\partial z}}{t_{\lambda}(y,z)}$$

$$\frac{\partial \rho_{w}(\lambda)}{\partial z} = -\frac{\frac{\partial \left(\zeta_{\lambda}(y,z)C_{\Delta P}+(\lambda,y,z)\right)}{\partial z}\rho_{R}(\lambda) + \rho_{w}(\lambda)\frac{\partial t_{\lambda}(y,z)}{\partial z}}{t_{\lambda}(y,z)}$$
(31)

In the derivative  $\partial(\zeta_{\lambda}C_{\Delta P}^{+})$ , we have checked on a large range of data that term  $\zeta_{\lambda}\partial C_{\Delta P}^{+}$ can be neglected with respect to term  $C_{\Delta P} + \partial \zeta_{\lambda}$  (it is often about 1%), so that  $C_{\Delta P} + can be$ considered as constant in the error propagation, if we wish to simplify the computation. It



Pixel-by-pixel uncertainty propagation in OLCI clear water branch

Ref.: S3-L2-SD-01-C01-ACR-TN

Version: 2.0

Date: 28/06/2013

Page: 18

could be however rigorously considered. The remaining derivatives  $\frac{\partial \zeta_{\lambda}}{\partial y}$ ,  $\frac{\partial \zeta_{\lambda}}{\partial z}$ ,  $\frac{\partial t_{\lambda}}{\partial y}$  and  $\frac{\partial t_{\lambda}}{\partial z}$  are moved to Appendix A; all terms can be computed analytically from quantities already expressed in the atmospheric correction scheme, except the tabulated transmittance, where we use an approximate exponential decay with respect to optical thickness.

Interestingly, we can develop the matrix product of  $var(\rho_w(\lambda))$  in order to separate the different contributions in the total uncertainty:

$$var(\rho_{w}(\lambda)) = \underbrace{\left(\frac{\sigma_{\lambda}}{t_{\lambda}}\right)^{2}}_{(c1)} + \underbrace{\frac{\sigma_{865}^{2} * C_{\Delta P}^{2} - (865)}{\rho_{R}^{2}(865)} \left(\frac{\partial \rho_{w}(\lambda)}{\partial z}\right)^{2}}_{(c2)} + \underbrace{\frac{\sigma_{779}^{2} * C_{\Delta P}^{2} - (779)}{\rho_{R}^{2}(779)} \left(\frac{\partial \rho_{w}(\lambda)}{\partial y}\right)^{2}}_{(c3)} + \underbrace{2 \left(\frac{\sigma_{779,865} * C_{\Delta P} - (779) * C_{\Delta P} - (865)}{\rho_{R}(779)\rho_{R}(865)}\right) \frac{\partial \rho_{w}(\lambda)}{\partial y} \frac{\partial \rho_{w}(\lambda)}{\partial z}}_{(c4)} + \underbrace{2 \left(\frac{\sigma_{\lambda,865} * C_{\Delta P} - (865)}{t_{\lambda}\rho_{R}(865)} \frac{\partial \rho_{w}(\lambda)}{\partial z}\right) + \underbrace{2 \left(\frac{\sigma_{\lambda,779} * C_{\Delta P} - (779)}{t_{\lambda}\rho_{R}(779)} \frac{\partial \rho_{w}(\lambda)}{\partial y}\right)}_{(c6)}}_{(c6)}$$

$$(32)$$

Term (c1) expresses the well-known fact that a TOA uncertainty at a given band  $\lambda$  in the visible produces same uncertainty on marine reflectance, inversely weighted by the total transmittance. This is often used to propagate TOA bias to marine reflectance bias (e.g. when the marine signal propagated TOA represents 10% of total signal, a 0.5% TOA bias yields to a 5% bias at sea level), but here it must be understood as uncertainty, not systematic bias. This gives the minimal reachable error if there would be no uncertainty propagation from the NIR bands.

In the NIR, this expression shows that if there is a perfect correlation between the TOA uncertainty at 779 and 865 nm, then terms (c2), (c3) and (c4) sums up to a minimal contribution:

$$\left(\frac{\sigma_{779} * C_{\Delta P} - (779)}{\rho_R(779)} \frac{\partial \rho_w(\lambda)}{\partial y} + \frac{\sigma_{865} * C_{\Delta P} - (865)}{\rho_R(865)} \frac{\partial \rho_w(\lambda)}{\partial z}\right)^2$$

By construction of the aerosol detection scheme, a positive error at 865 nm tends lower the difference with signal at 779 nm, hence decrease the Angstrom exponent, what is similar as a negative error at 779 nm. This means that terms  $\frac{\partial \rho_w(\lambda)}{\partial y}$  and  $\frac{\partial \rho_w(\lambda)}{\partial z}$  have opposite signs, and may partially compensiate in sum (c2)+(c3)+(c4) as well as in sum (c5)+(c6). This will be illustrate on real data.



Pixel-by-pixel uncertainty propagation in OLCI clear water branch

Ref.: S3-L2-SD-01-C01-ACR-TN

Version: 2.0

Date: 28/06/2013

Page: 19

#### 5.2 Bio-optical data uncertainty

The ocean colour products mentioned in section 3.2 are all expressed as functions of two water reflectances. The mathematical framework given in introduction can be applied in a simpler way with the variance-covariance matrix of the two reflectances as input errors.

OC4Me Chl- $\alpha$  - From the formulation of the OC4Me algorithm, the derivatives of chlorophyll with respect to  $R_1$  and  $R_2$  are:

$$\frac{\partial Chl}{\partial R_1} = \frac{Chl}{R_1} \sum_{i=1}^{N} A_i * i * \left(\log_{10} \frac{R_1}{R_2}\right)^{i-1}$$
(33)

and

$$\frac{\partial Chl}{\partial R_2} = -\frac{Chl}{R_2} \sum_{i=1}^{N} A_i * i * \left(\log_{10} \frac{R_1}{R_2}\right)^{i-1}$$
(34)

which leads to the analytical formulation:

$$\sigma_{\text{Chl}}^2 = \text{Chl}^2 * \left( \sum_{i=1}^{N} A_i * i * \left( \log_{10} \frac{R_1}{R_2} \right)^{i-1} \right)^2 * \left( \frac{\sigma_{R_1}^2}{R_1^2} - 2 \frac{\sigma_{R_1 R_2}}{R_1 R_2} + \frac{\sigma_{R_2}^2}{R_2^2} \right)$$
(35)

This formula shows that the uncertainty on chlorophyll is weaker when the uncertainties on  $R_1$  and  $R_2$  are correlated. In case of a perfect correlation, the uncertainty is minimum with

$$\sigma_{\text{Chl}}^{2} = \text{Chl}^{2} * \left( \sum_{i=1}^{N} A_{i} * i * \left( \log_{10} \frac{R_{1}}{R_{2}} \right)^{i-1} \right)^{2} * \left( \frac{\sigma_{R_{1}}}{R_{1}} - \frac{\sigma_{R_{2}}}{R_{2}} \right)^{2} \quad \text{when } \sigma_{R_{1}R_{2}} = \sigma_{R_{1}}\sigma_{R_{2}}$$
 (36)

Moreover, the uncertainty vanishes if the input uncertainties are close in relative values (i.e.  $\frac{\sigma_{R_1}}{R_1} \approx \frac{\sigma_{R_2}}{R_2}$ ); this analytical computations retrives the known interest of band ratio algorithms and justifies the need of relative errors comparable between water reflectances in the blue and the green.

OK2-560 Kd490 - The same methodology applied to OK2-560 algorithm formula yields:

$$\sigma_{K_d 490}^2 = \left(K_d(490) - K_w(490)\right)^2 * \left(\sum_{i=1}^N B_i * i * \left(\log_{10} \frac{R_{490}}{R_{560}}\right)^{i-1}\right)^2 * \left(\frac{\sigma_{R_{490}}^2}{R_{490}^2} - 2\frac{\sigma_{R_{490}R_{560}}}{R_{490}R_{560}} + \frac{\sigma_{R_{560}}^2}{R_{560}^2}\right)$$
(37)

Secchi depth transparency – Now the input uncertainty  $\sigma_{\rho}$  is defined on normalised marine reflectance and propagates to Secchi disk depth by



Pixel-by-pixel uncertainty propagation in OLCI clear water branch

Ref.: S3-L2-SD-01-C01-ACR-TN

Version: 2.0

Date: 28/06/2013

Page: 20

$$\sigma_{Z_{sd}}^{2} = \left(\frac{\partial Z_{sd}}{\partial \rho_{wN}(490)}, \frac{\partial Z_{sd}}{\partial \rho_{wN}(560)}\right) * \begin{pmatrix} \sigma_{\rho_{490}}^{2} & \sigma_{\rho_{490}\rho_{560}} \\ \sigma_{\rho_{490}\rho_{560}} & \sigma_{\rho_{560}}^{2} \end{pmatrix} * \begin{pmatrix} \frac{\partial Z_{sd}}{\partial \rho_{wN}(490)} \\ \frac{\partial Z_{sd}}{\partial \rho_{wN}(560)} \end{pmatrix}$$
(38)

with

$$\frac{\partial Z_{sd}}{\partial \rho_{wN}(490)} = \left(-\alpha_{490} \frac{R_{sd}}{R^{-}(490)(R_{sd} - R^{-}(490))} \frac{Z_{sd}}{\gamma} + \gamma \frac{a}{R^{-}(560)}\right) * \frac{A_{490}}{(A_{490} + B_{490}R^{-}(490))^{2}}$$
(39)

and

$$\frac{\partial Z_{sd}}{\partial \rho_{wN}(560)} = \left(-\alpha_{560} \frac{R_{sd}}{R^{-}(560)(R_{sd} - R^{-}(560))} \frac{Z_{sd}}{\gamma} - \gamma \frac{aR^{-}(490)}{R^{-}(560)^{2}}\right) * \frac{A_{560}}{\left(A_{560} + B_{560}R^{-}(560)\right)^{2}}$$

$$(40)$$

Contrary to previous algorithms, there is no obvious error cancellation  $\sigma_{Z_{sd}}^2$  even when uncertainty on  $\rho_{wN}(490)$  and  $\rho_{wN}(560)$  are correlated.

#### 5.3 Validation

We have implemented the uncertainties calculation in the MERIS Level 2 ground segment code available in the ODESA software (http://earth.eo.esa.int/odesa). The validation is based on the SPG and SIO macropixels (5x5 RR) studied previously, in order to get estimate of TOA radiometric variances and covariances. These input uncertainties are assigned to the central pixel of the macropixel and propagated to get estimated uncertainties on  $\rho_w$ , then  $\mathit{Chl}$ ,  $\mathit{K}_d(490)$  and  $\mathit{Z}_{\mathit{sd}}$ . In parallel, the spatial variance and covariance of these quantities is assessed on the 25 pixels and is considered as the real (observed) uncertainties. The uncertainty estimate is compared to this a posteriori statistics.

#### 5.3.1 Validation of marine reflectance uncertainties

Figure 5, Figure 6, Figure 7, and Figure 8 show the excellent agreement between observed and computed uncertainties at bands at 412, 490, 560, and 709 nm (other terms behave as well). The correlation coefficient is always higher than 0.93 and the slopes close to 1. The comparison is even better when going closer to the red part of the spectrum, what is probably due to a weaker approximation of the transmittances there. Note that scales are different between standard-deviation  $\sigma(\rho_w(\lambda))$  and covariance  $cov\left(\rho_w(\lambda_i), \rho_w(\lambda_j)\right)$ .



Pixel-by-pixel uncertainty propagation in OLCI clear water branch

Ref.: S3-L2-SD-01-C01-ACR-TN

Version: 2.0

Date: 28/06/2013

Page: 21

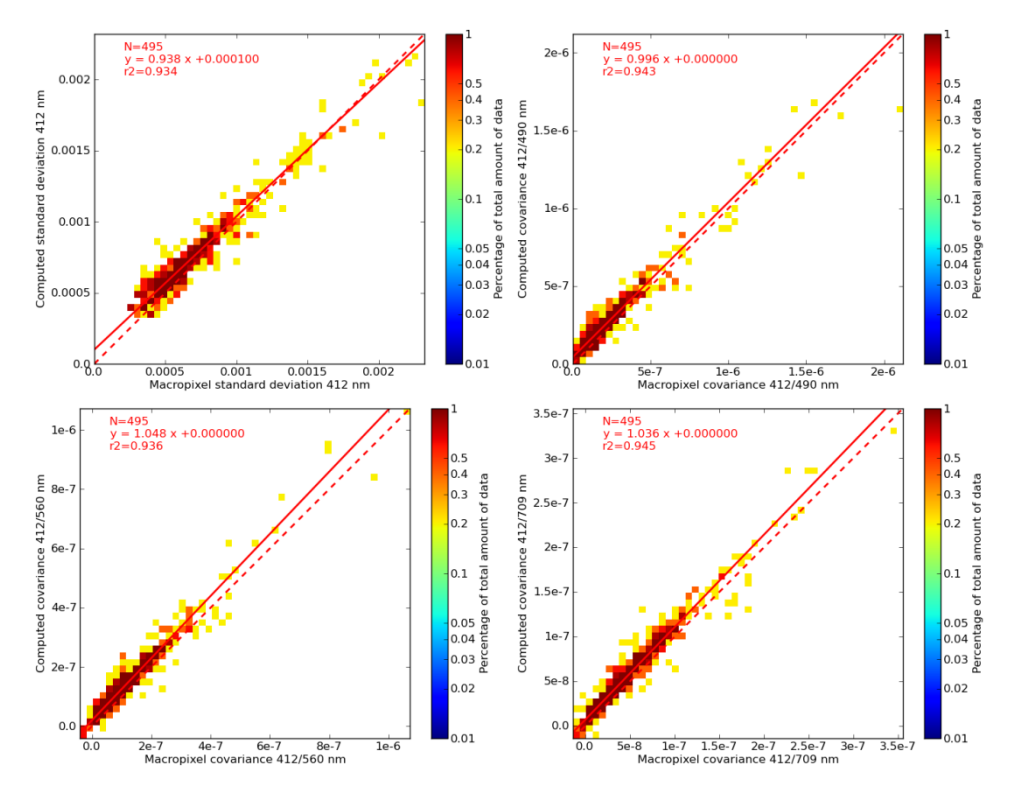


Figure 5: Comparison between observed (x-axis) and computed (y-axis) uncertainties in marine reflectance; from left to right and top to bottom:  $(\rho_w(412))$ ,  $cov(\rho_w(412),\rho_w(490))$ ,  $cov(\rho_w(412),\rho_w(560))$  and  $cov(\rho_w(412),\rho_w(709))$ .

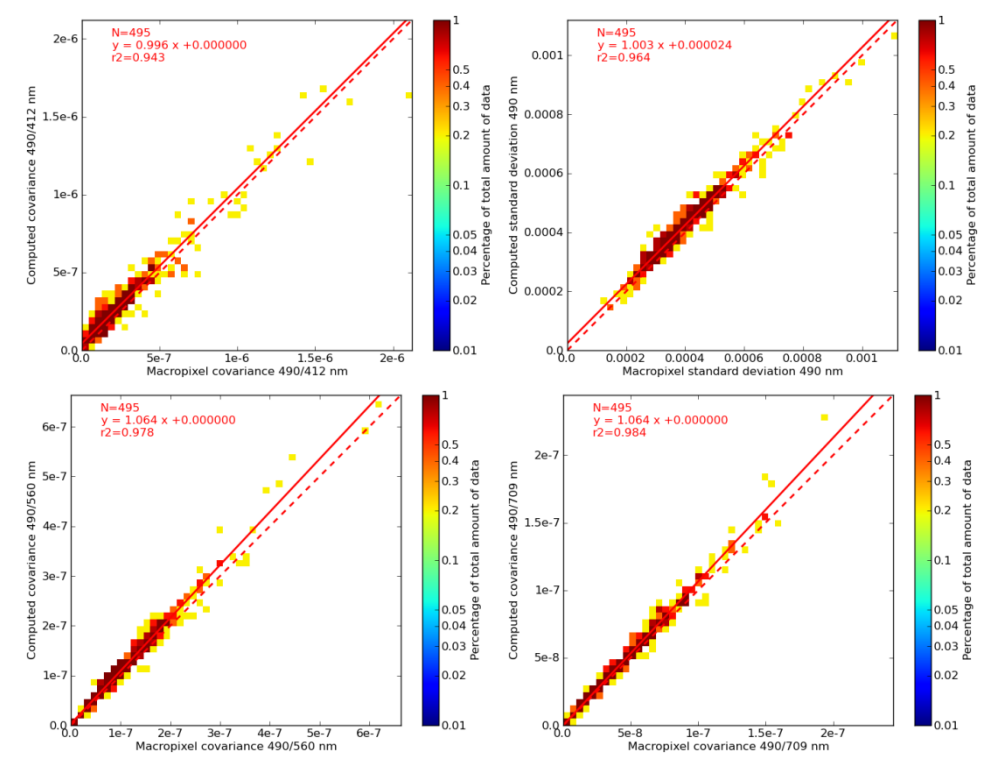


Figure 6: Comparison between observed (x-axis) and computed (y-axis) uncertainties in marine reflectance; from left to right and top to bottom:  $cov(\rho_w(490), \rho_w(412))$ ,  $\sigma(\rho_w(490))$ ,  $cov(\rho_w(490), \rho_w(560))$  and  $cov(\rho_w(490), \rho_w(709))$ .



Pixel-by-pixel uncertainty propagation in OLCI clear water branch

Ref.: S3-L2-SD-01-C01-ACR-TN

Version: 2.0

Date: 28/06/2013

Page: 22

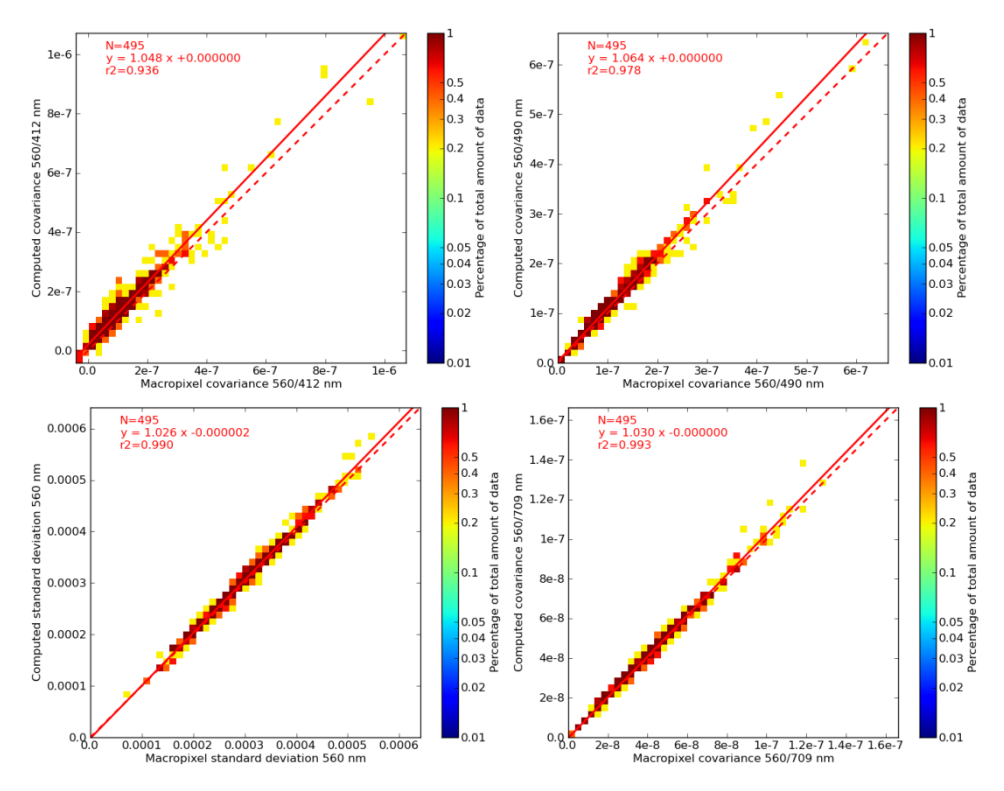


Figure 7: Comparison between observed (x-axis) and computed (y-axis) uncertainties in marine reflectance; from left to right and top to bottom:  $v(\rho_w(560), \rho_w(412)) cov(\rho_w(560), \rho_w(490))$ ,  $\sigma(\rho_w(560))$ , and  $cov(\rho_w(560), \rho_w(709))$ .

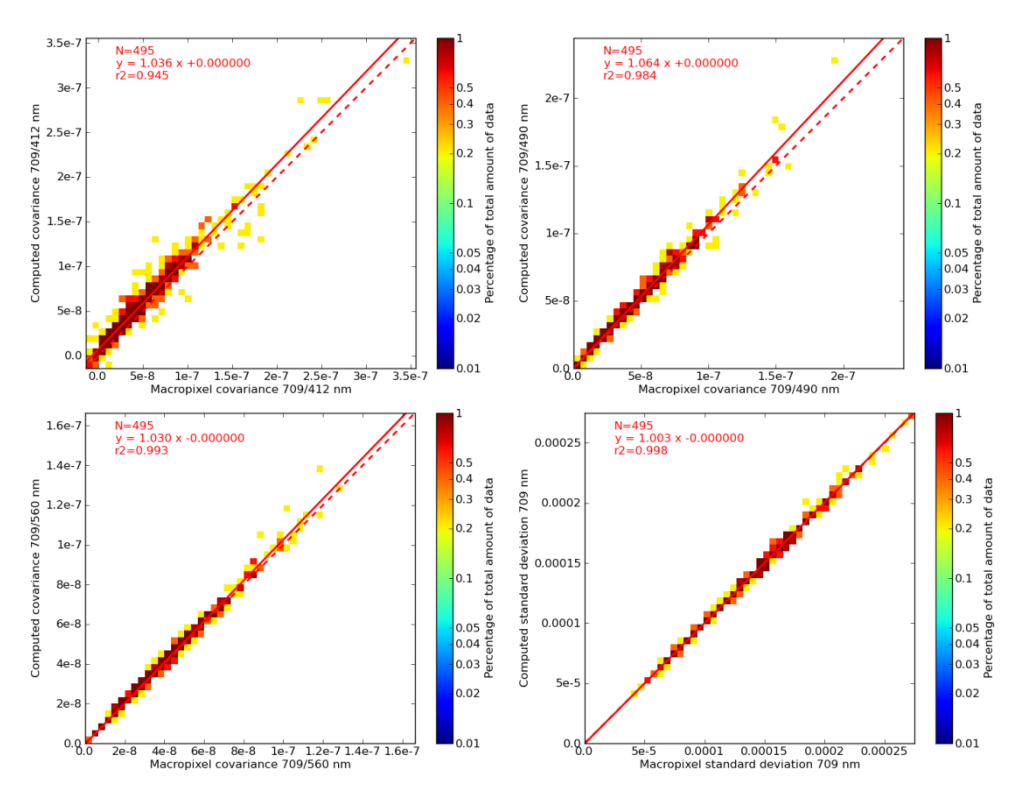


Figure 8: Comparison between observed (x-axis) and computed (y-axis) uncertainties in marine reflectance; from left to right and top to bottom:  $ov(\rho_w(709), \rho_w(412)), cov(\rho_w(709), \rho_w(490)), cov(\rho_w(560), \rho_w(709))$  and  $\sigma(\rho_w(709))$ 



Pixel-by-pixel uncertainty propagation in OLCI clear water branch

Ref.: S3-L2-SD-01-C01-ACR-TN

Version: 2.0

Date: 28/06/2013

Page: 23

At this point we stress the importance of considering the TOA covariance terms in the computation of water reflectance uncertainties. Doing the same analysis but without considering extral-diagonal terms in equation (26) leads to a highly overestimated uncertainty, shown for example at 412 nm in Figure 9.

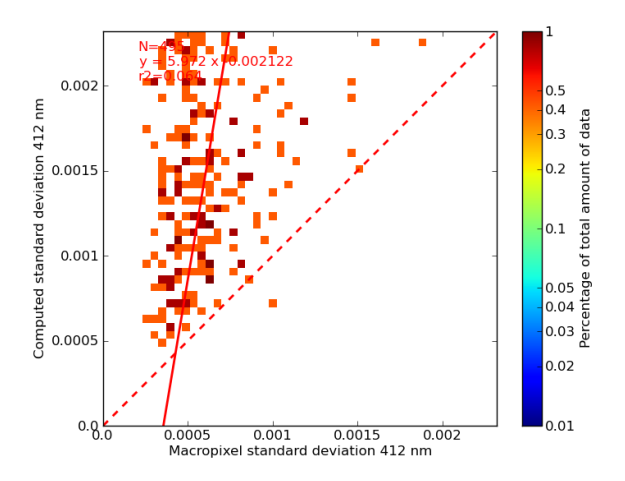


Figure 9: Degraded comparison between observed (x-axis) and computed (y-axis) uncertainties in marine reflectance at 412 nm (standard deviation) when the TOA covariance terms are not included

These results prove the validity of the noise propagation in atmospheric correction as well as the importance of considering all matrix terms characterising the TOA uncertainty.

#### 5.3.2 Validation of Chl, Kd and Zsd uncertainties

We conduct a similar analysis on the ocean colour products, using the uncertainties reviously found on the marine reflectance. This means the validation is end-to-end, starting from TOA uncertainties.

Figure 10 (left) compares the computed uncertainty on ChI against the macropixel standard-deviation and shows a very good agreement. Hence we manage to directly link the chlorophyll noise to TOA radiometric noise, contrary to Hu et~al.~2012 on MERIS data (the reason of failure in this reference still remains unexplicated). On right figure, we again demonstrate the importance of the input covariance uncertainty (now from marine reflectance), which allows to decrease the independent errors due to blue and green and to retrieve the proper estimate. Hence it is crucial to compute in the processing chain all necessary terms  $cov\left(\rho_w(\lambda_i),\rho_w(\lambda_j)\right)$ , although only the variance  $var\left(\rho_w(\lambda)\right)$  are planned to be provided as OLCI Level 2 outputs.



Pixel-by-pixel uncertainty propagation in OLCI clear water branch

Ref.: S3-L2-SD-01-C01-ACR-TN

Version: 2.0

Date: 28/06/2013

Page: 24

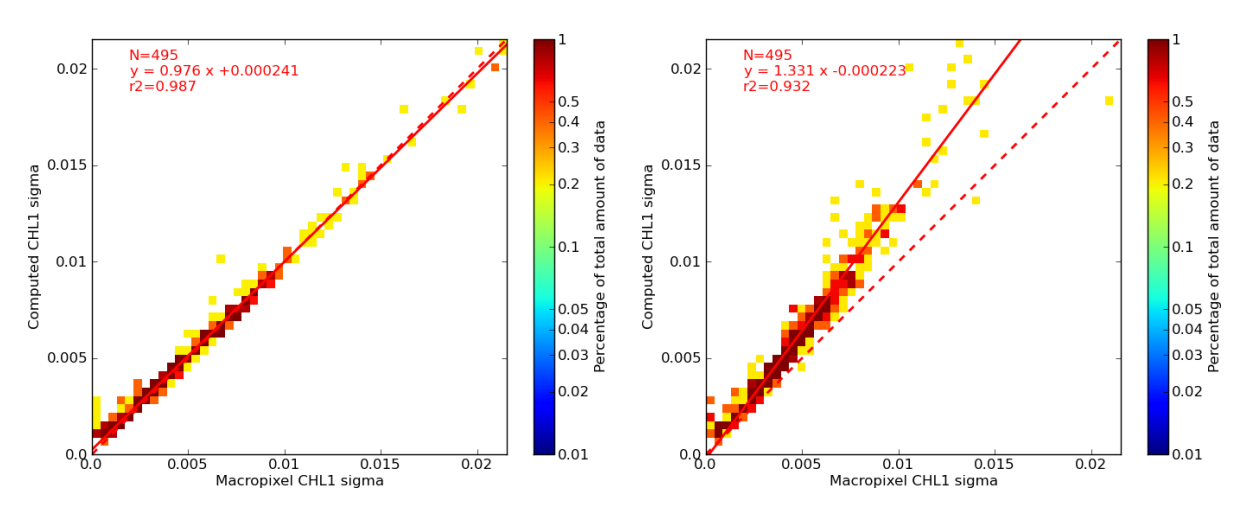


Figure 10: Comparison between observed (x-axis) and computed (y-axis) Chl uncertainty, with the complete formulation (left) and when when neglecting the marine reflectance covariance terms (right).

Validation of Kd490 uncertainty is similar, with a perfect comparison between observed and computed values (Figure 11).

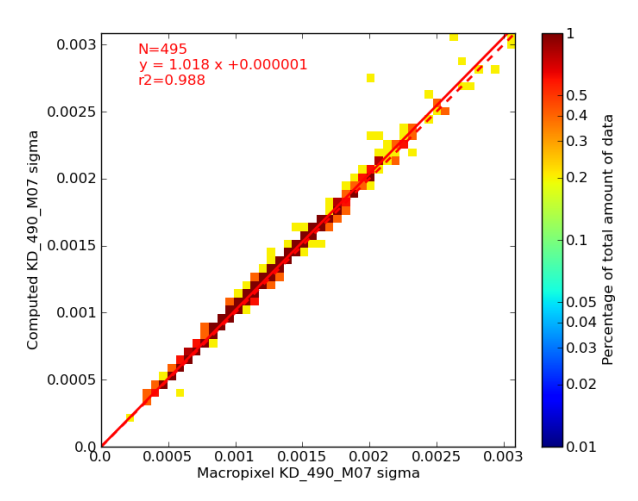


Figure 11: Comparison between observed (x-axis) and computed (y-axis) Kd490 uncertainty.

Eventually regarding Secchi depth, validation of uncertainty estimate is again very satisfying (Figure 12), with however a slightly weaker correlation slope.



Pixel-by-pixel uncertainty propagation in OLCI clear water branch

Ref.: S3-L2-SD-01-C01-ACR-TN

Version: 2.0

Date: 28/06/2013

Page: 25

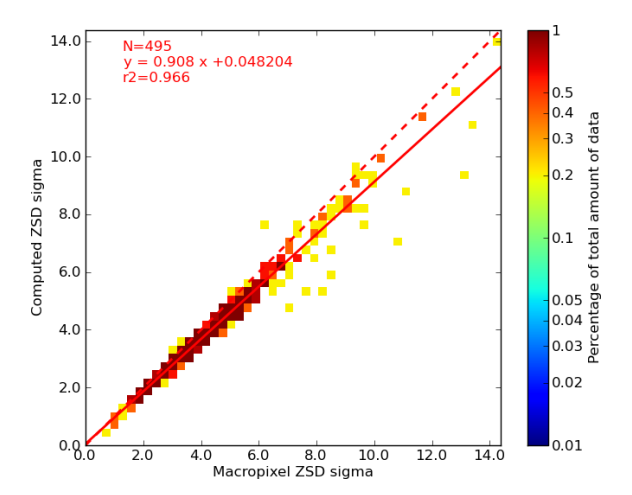


Figure 12: Validation of the computed  $Z_{sd}$  uncertainty (Y axis) against macropixel statistics (X axis).

All these results validate the determination and implementation of the error propagation in OLCI Case-1 ocean colour products.



Pixel-by-pixel uncertainty propagation in OLCI clear water branch

Ref.: S3-L2-SD-01-C01-ACR-TN

Version: 2.0

Date: 28/06/2013

Page: 26

#### 6 MERIS uncertainty maps over the Open Ocean

#### 6.1 Method

We here apply our methodology on full MERIS scenes and draw pixel-by-pixel uncertainties maps. In order to satisfy our working assumption, the analysis is based on deep water zones, where the bright pixel atmospheric correction plays no role, and out of the glint contamination. The uncertainty propagation starts just before the clear-water atmospheric correction, i.e. on  $\rho_{gc}$ , as in the previous validation exercise. However now we cannot consider homogeneous target to locally determine the input TOA uncertainty. This pixel-by-pixel input noise at Level1 being not available to date, we consider a square-root shape with reference uncertainties at a typical signal  $L_{ref}$ , converted in reflectance unit:

$$\sigma_{\lambda} = \frac{\sqrt{\frac{\pi L_{ref}(\lambda)}{F_0(\lambda)\cos\theta_s}}}{SNR_{ref}}\sqrt{\rho(\lambda)}$$
(41)

The reference signal  $L_{ref}$  and  $SNR_{ref}$  are taken from Delwart, 2008 (see table below). The covariance terms  $\sigma_{\lambda i,\lambda j}$  are derived from these  $\sigma_{\lambda}$  through formula

$$\sigma_{\lambda i,\lambda j} = r_{\lambda i,\lambda j} \, \sigma_{\lambda i} \, \sigma_{\lambda j} \tag{42}$$

assuming that the mean correlations  $r_{\lambda i,\lambda j}$  found previously on the oligotrophic sites are a characteristic of the sensor (see Figure 13). Clearly these are assumptions on the exact Level 1 uncertainties, and yet realistic they would have to be checked by other dedicated and independent studies.

Table 1: MERIS reference signal  $L_{ref}$  and associated SNR (in reduced resolution) from Delwart 2008

λ (nm)	$L_{ref}$ (at $ heta_{ m s}=45^{\circ})$ (mW /m²/nm/sr)	$SNR_{ref}$
412	81.0	1068
443	70.0	1048
490	53.0	1080
510	45.3	1051
560	31.4	938
620	20.4	714
665	15.5	708
681	14.1	500
709	11.9	616
754	9.5	522
779	8.5	766
865	5.3	524



Pixel-by-pixel uncertainty propagation in OLCI clear water branch

Ref.: S3-L2-SD-01-C01-ACR-TN

Version: 2.0

Date: 28/06/2013

Page: 27

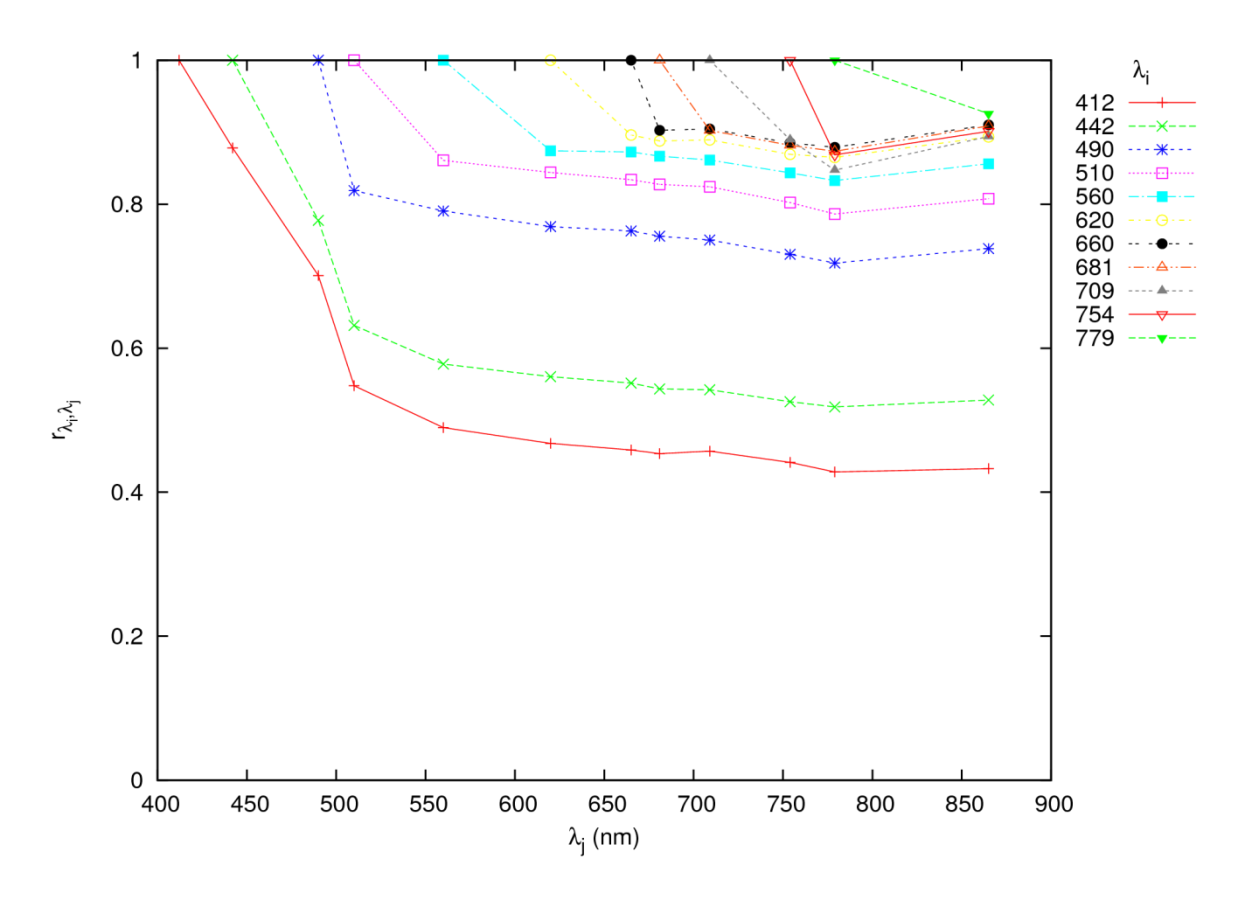


Figure 13: Mean correlation coefficient  $r_{\lambda i,\lambda j}$  between band  $\lambda i$  (colours) and  $\lambda j$  (x-axis) as computed on oligotrophic sites.

Two test scenes are chosen: one over the South Pacific Gyre ( $16^{th}$  June 2007,  $\theta_s$  ranging from 54° to 67°) and one over Hawaii ( $13^{th}$  September 2003,  $\theta_s$  around 33° outside the sun glint region). Level 1 composite and aerosol products are provided on Figure 14. No marine signal in the NIR is expected in such areas, but the atmosphere presents various patterns, in particular over the Hawaii scene where Angstrom coefficient can reach 2 on aerosol plume off the islands (yet no visible on the Level 1 product). In all subsequent figures the MERIS high glint pixels are masked in black.



Pixel-by-pixel uncertainty propagation in OLCI clear water branch

Ref.: S3-L2-SD-01-C01-ACR-TN

Version: 2.0

Date: 28/06/2013

Page: 28

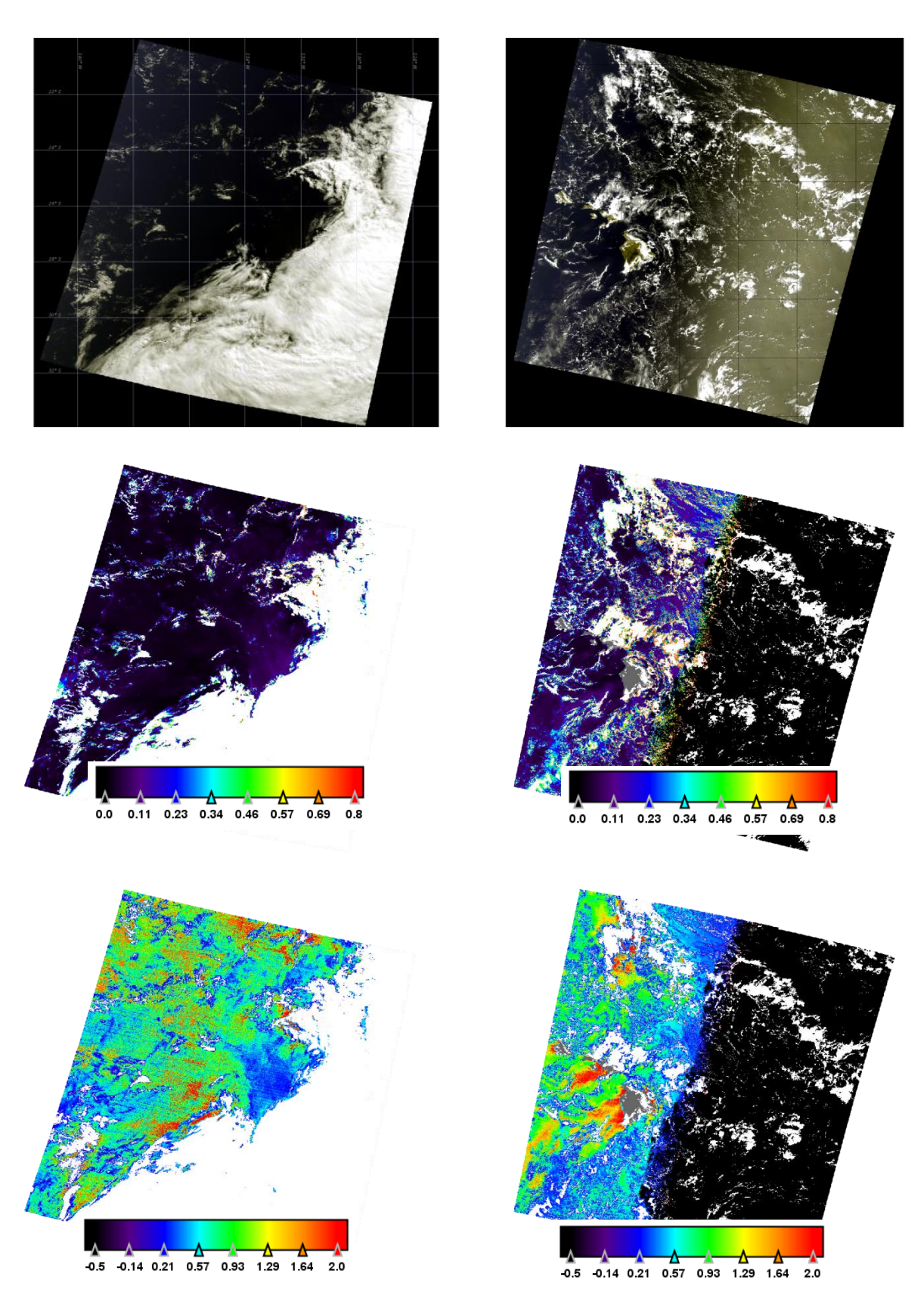


Figure 14: MERIS test scenes over South Pacific Gyre (left) and Hawaii (right): Level 1 composite (top), aerosol optical thickness at 865 nm (middle) and Angstrom coefficient (bottom).



Pixel-by-pixel uncertainty propagation in OLCI clear water branch

Ref.: S3-L2-SD-01-C01-ACR-TN

Version: 2.0

Date: 28/06/2013

Page: 29

#### **6.2** Uncertainty maps

Marine reflectance  $\rho_w$  at bands 412, 490 and 560 nm and associated uncertainties  $\sigma = \sqrt{var(\rho_w)}$  are displayed on Figure 15 for SPG and Figure 16 for Hawaii, with same color scales.

Over SPG we observe a continuous gradient of uncertainty with air mass, ranging from about  $3.0 \times 10^{-4}$  to  $4.5 \times 10^{-4}$  at 412 nm,  $1.5 \times 10^{-4}$  to  $2.0 \times 10^{-4}$  at 490 nm and  $0.9 \times 10^{-4}$  to  $1.4 \times 10^{-4}$  at 560 nm. Furthermore patchy higher values appear in some part of the scene (particulary middle and top) as well as along clouds edges, reaching more than  $6.0 \times 10^{-4}$  at 412 nm,  $3.0 \times 10^{-4}$  at 490 nm and  $2.0 \times 10^{-4}$  at 560 nm. It is noticeable that the Eastern rectangular zone surrounded by the large cloud does not present any of these high uncertainties.

Over Hawaii, the background uncertainty is spatially homogeneous and lower, of about  $3.0 \times 10^{-4}$  at 412 nm,  $1.3 \times 10^{-4}$  at 490 nm and less than  $1.0 \times 10^{-4}$  at 560 nm. However higher uncertainties also appear around clouds, and most interestingly large values are observed over the plume detected by high Angstrom coefficients (see Figure 15). Note that these uncertainties appear even if aerosol content is low ( $\tau_a(865) < 0.05$ ).

In term of relative values, these uncertainties are generally within 2% of the marine signal.

On Figure 17 we show that high patchy values (typically  $\sigma(490)>2.0x10^{-4}$ ) correspond well to pixels flagged by PCD\_1\_13 (uncertain marine reflectance) or OADB (no bracketing aerosol models). This means that the uncertainty estimate can be used as a tool to refine the Level 2 flags, providing users a continuous confidence level that can be thresholded according to one's needs.



Pixel-by-pixel uncertainty propagation in OLCI clear water branch

Ref.: S3-L2-SD-01-C01-ACR-TN

Version: 2.0

Date: 28/06/2013

Page: 30

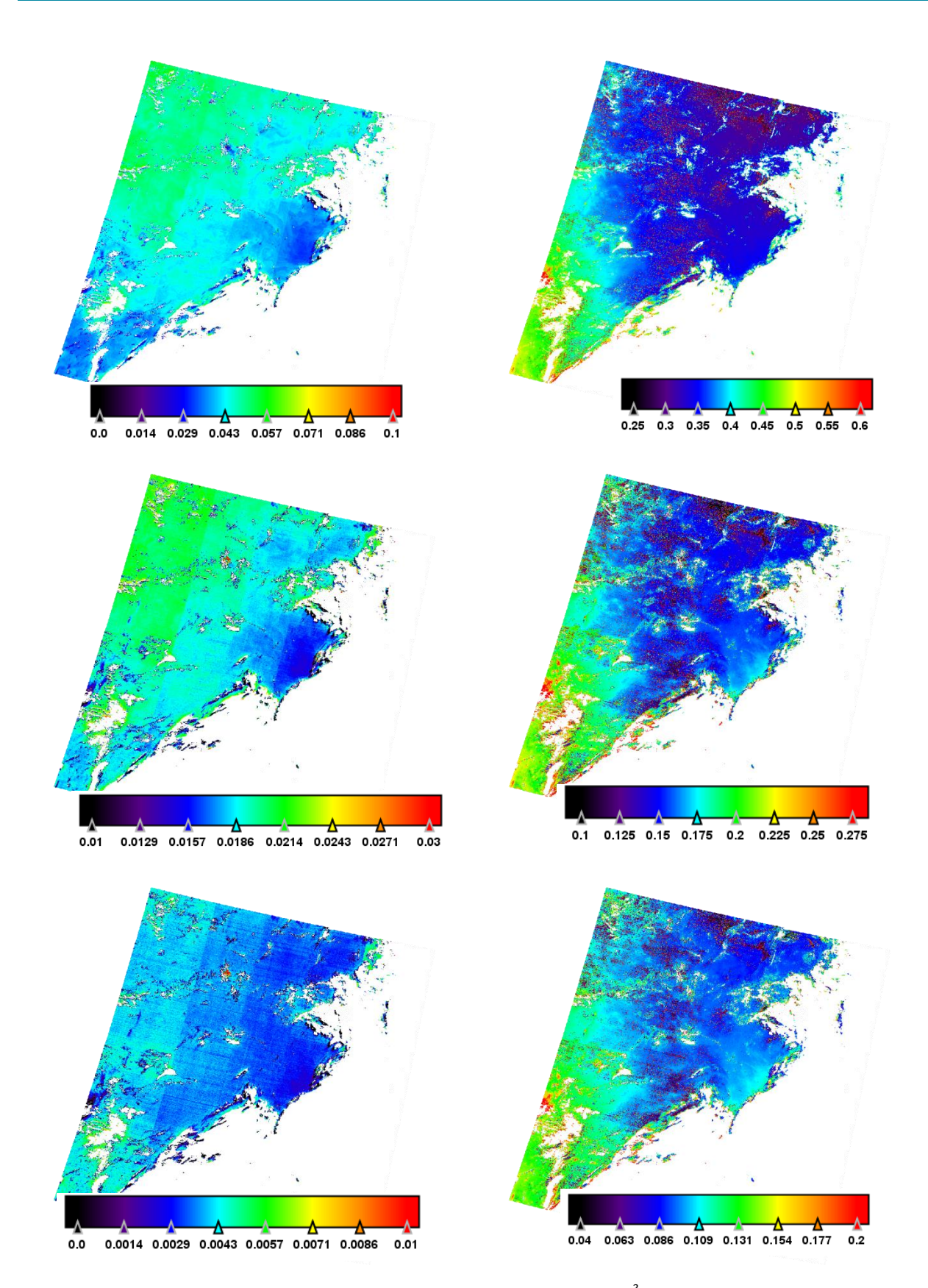


Figure 15: MERIS marine reflectance (left) and associated uncertainties x10<sup>3</sup> (right) at bands 412, 490 and 560 (top to bottom) over South Pacific Gyre



Pixel-by-pixel uncertainty propagation in OLCI clear water branch

Ref.: S3-L2-SD-01-C01-ACR-TN

Version: 2.0

Date: 28/06/2013

Page: 31

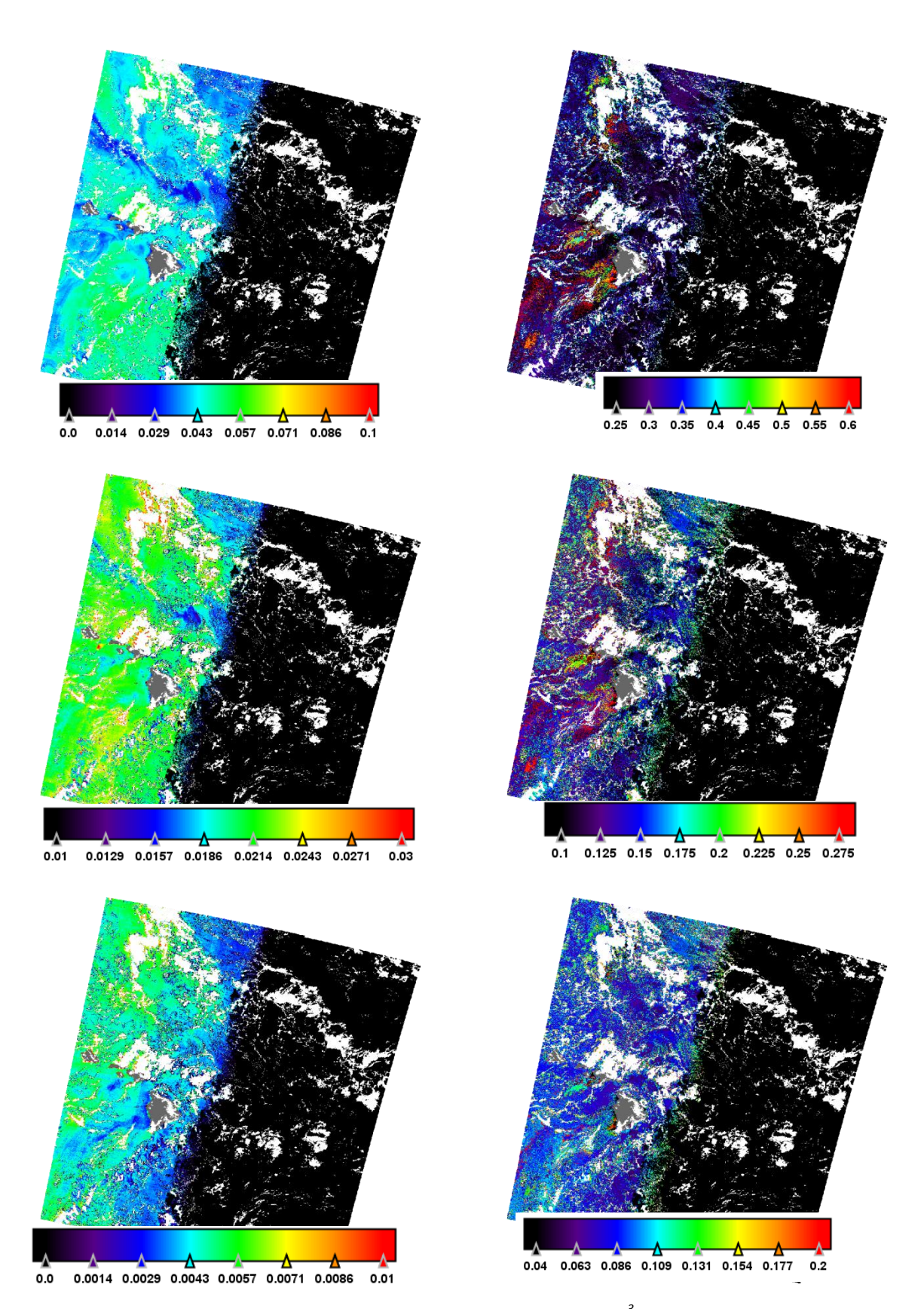


Figure 16: MERIS marine reflectance (left) and associated uncertainties x10<sup>3</sup> (right) at bands 412, 490 and 560 (top to bottom) over Hawaii

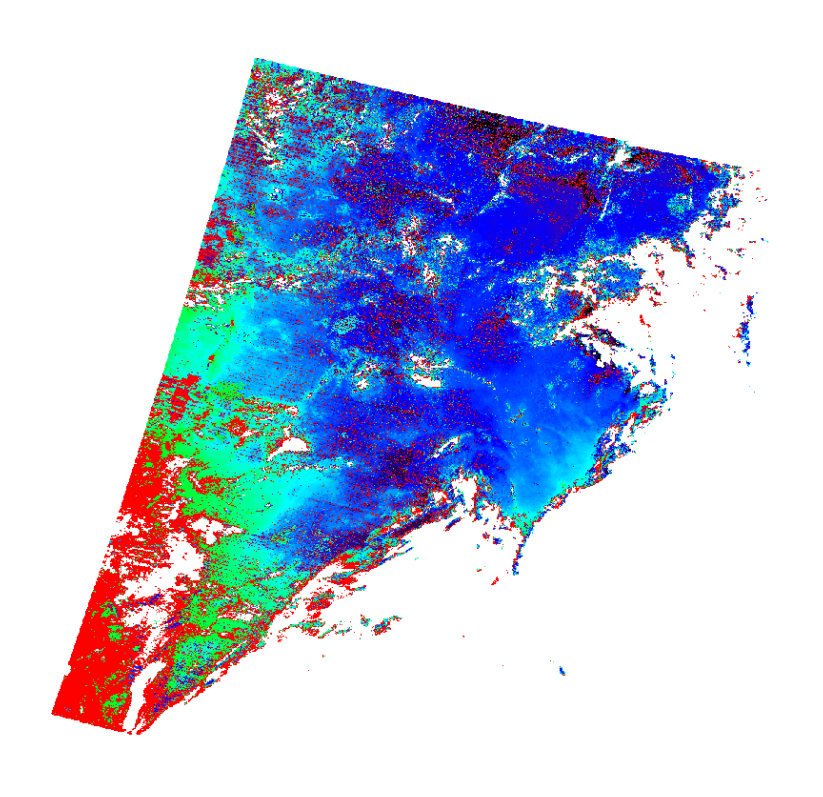


Pixel-by-pixel uncertainty propagation in OLCI clear water branch

Ref.: S3-L2-SD-01-C01-ACR-TN

Version: 2.0

Date: 28/06/2013



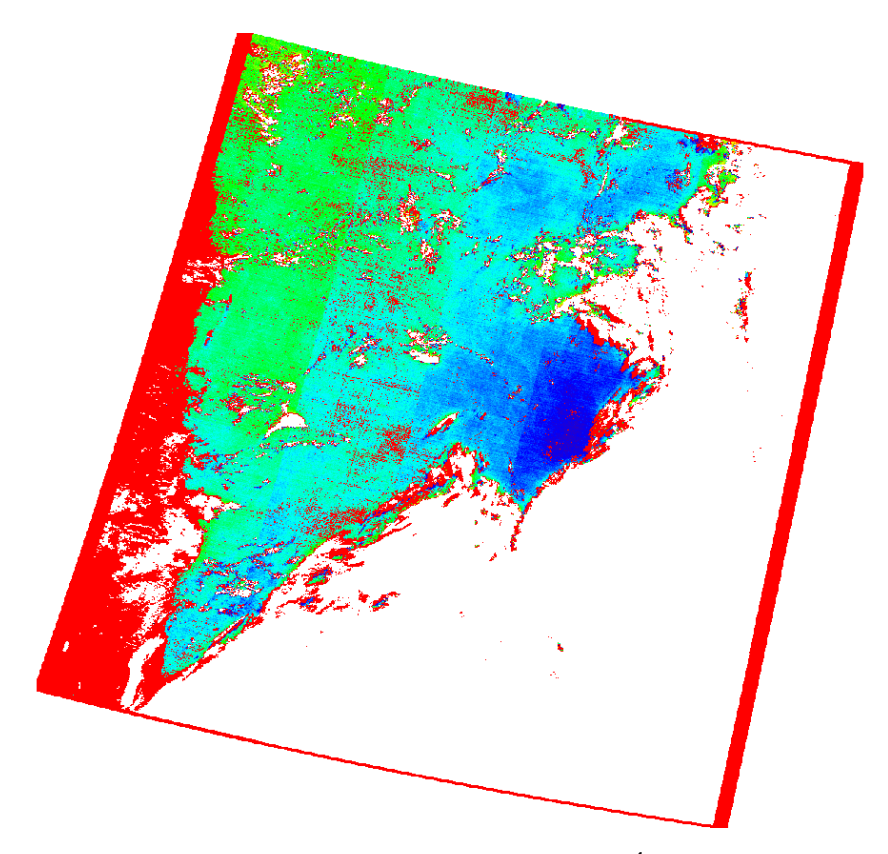


Figure 17: Comparison between  $\rho_w(490)$  uncertainties higher than  $2x10^4$  (top, in red) and {PCD\_1\_13 or OADB} flags (bottom, in red; background is  $\rho_w(490)$ )



Pixel-by-pixel uncertainty propagation in OLCI clear water branch

Ref.: S3-L2-SD-01-C01-ACR-TN

Version: 2.0

Date: 28/06/2013

Page: 33

Uncertainty maps on ocean colour products are provided on Figure 18 and Figure 19 for respectively SPG and Hawaii, again with same scale for both scenes. They are expressed in relative percentage (i.e  $\sigma_{Chl}/Chl$ ,  $\sigma_{Kd_{490}}/Kd_{490}$  and  $\sigma_{Z_{sd}}/Z_{sd}$ ).

Chlorophyll uncertainty is generally within 5%, occasionnally higher (up to 10 or 15%) but for very low concentration (lower than 0.03 mg/m³). Patchy high errors are reduced compared to marine reflectance, showing the interest of band ratio algorithm. Kd490 uncertainty is even smaller, always less than 2.5% except most noisy pixels at 4%. Secchi depth uncertainty is globally about the same level, but seems to be more sensitive to high reflectance noise (reaching 15% relative uncertainty on SPG scene for pixels having highest reflectance uncertainty); this was foreseen from equations (38)-(40) where error cancellation (if any) is not as effective as for simple band ratio algorithm.

Clearly, these numbers due to radiometric noise propagation are lower than model uncertainty in the bio-optical inversion (e.g. a factor two in chlorophyll concentration for a given band ratio, cf. figure 7 in Morel and Antoine, 2011). This means that ocean colour product uncertainties are mainly driven by error in modelling (including atmospheric error) and not by the remote-sensing sensor itself, when radiometric quality is as per MERIS instrument.



Pixel-by-pixel uncertainty propagation in OLCI clear water branch

Ref.: S3-L2-SD-01-C01-ACR-TN

Version: 2.0

Date: 28/06/2013

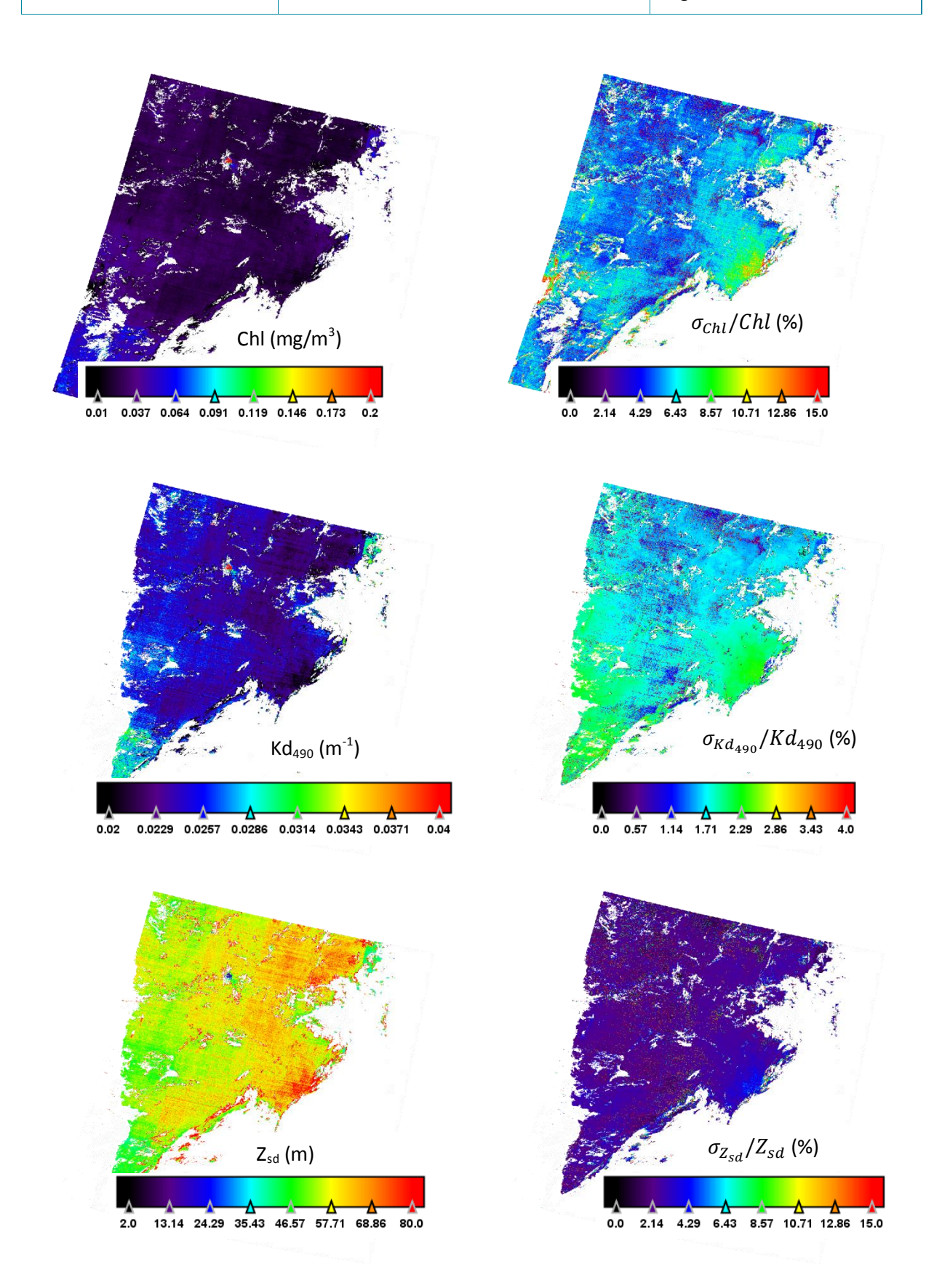


Figure 18: MERIS ocean colour products (left) and associated relative uncertainties (right, in %) at SPG; from top to bottom: chlorophyll  $(mg/m^3)$ , Kd490  $(m^{-1})$  and Secchi depth (m)



Pixel-by-pixel uncertainty propagation in OLCI clear water branch

Ref.: S3-L2-SD-01-C01-ACR-TN

Version: 2.0

Date: 28/06/2013

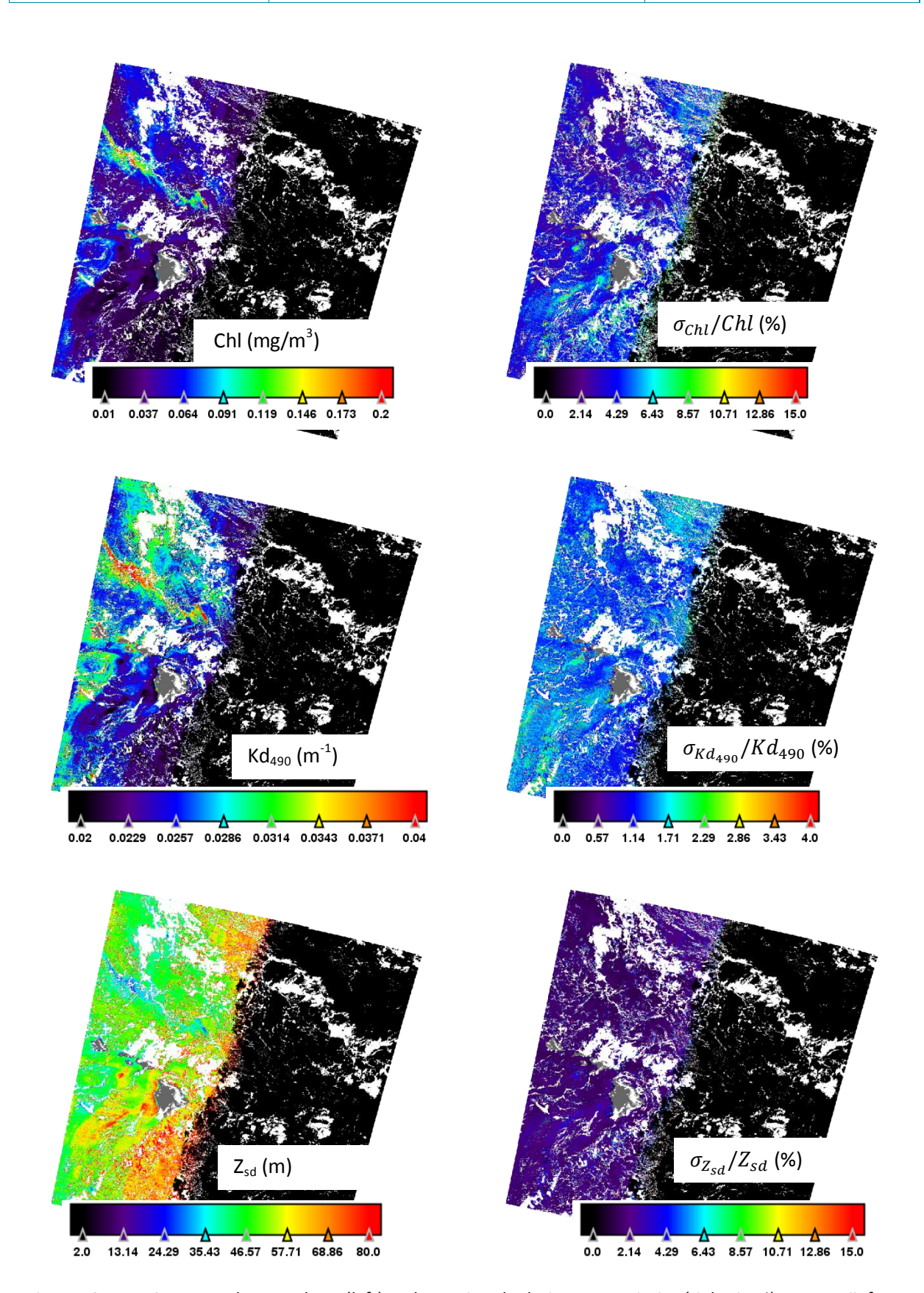


Figure 19: MERIS ocean colour products (left) and associated relative uncertainties (right, in %) at Hawaii; from top to bottom: chlorophyll (mg/m3), Kd490 (m-1) and Secchi depth (m)



Pixel-by-pixel uncertainty propagation in OLCI clear water branch

Ref.: S3-L2-SD-01-C01-ACR-TN

Version: 2.0

Date: 28/06/2013

Page: 36

#### 6.3 Discussion on uncertainty propagation by atmospheric correction

We have seen that marine reflectance uncertainties may grow because of large air mass (SPG case) and/or because high Angstrom exponent (Hawaii case). The latter effect can be directly related to the aerosol models detected by the atmospheric correction scheme. On Figure 20 there is a clear relationship between high uncertainties at 412 nm and selection of rural or so-called "blue" models.

The role of each band in the total uncertainty can be understood by adding progressively each contributor from equation (32). Figure 21 shows this decomposition over SPG:

- 1. The background uncertainty on marine reflectance comes from the TOA uncertainty at considered band, scaled by the total transmittance (hence total air mass);
- 2. Atmospheric correction propagate uncertainty at 865 nm, and in particular creates the strong pixel by pixel variability;
- 3. The 779 nm band also adds uncertainty for same reason; at this stage the resulting uncertainty is larger than the observed one's;
- 4. Adding the correlated noise betweent 865 and 775 nm cancels a large part of the uncertainty due to atmospheric correction but not all;
- 5. The correlated noise between 865 nm and the visible band increases again the estimate;
- 6. Same contribution from 779 nm, which has roughly an opposite sign, cancels the previous effect; this leads to the final uncertainty estimate.

These effects have been known for long in atmospheric correction of ocean colour data, but the interest of the current approach is to quantify accurately each of them.



Pixel-by-pixel uncertainty propagation in OLCI clear water branch

Ref.: S3-L2-SD-01-C01-ACR-TN

Version: 2.0

Date: 28/06/2013

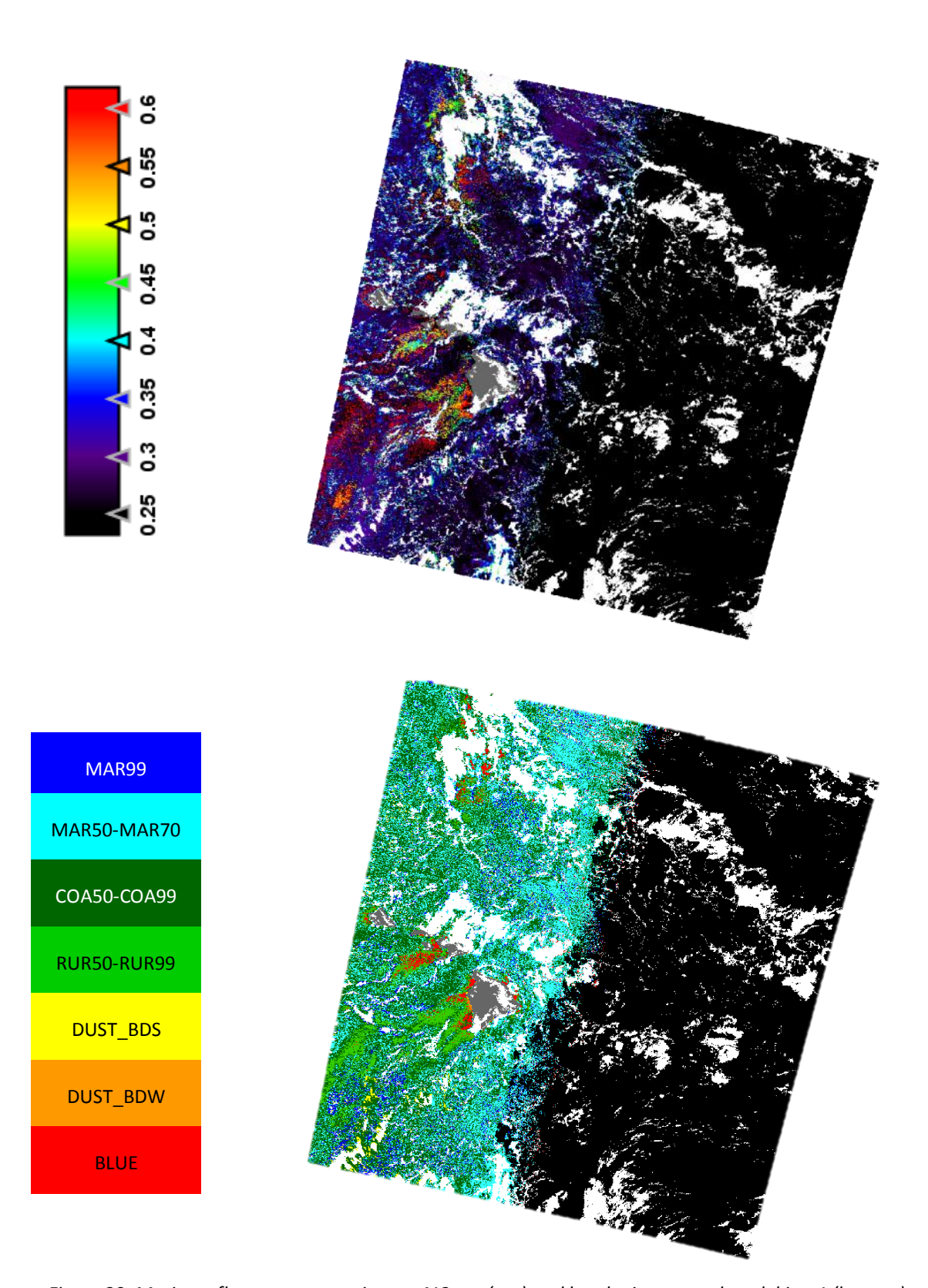


Figure 20: Marine reflectance uncertainty at 412 nm (top) and bracketing aerosol model iaer1 (bottom) over Hawaii



Pixel-by-pixel uncertainty propagation in OLCI clear water branch

Ref.: S3-L2-SD-01-C01-ACR-TN

Version: 2.0

Date: 28/06/2013

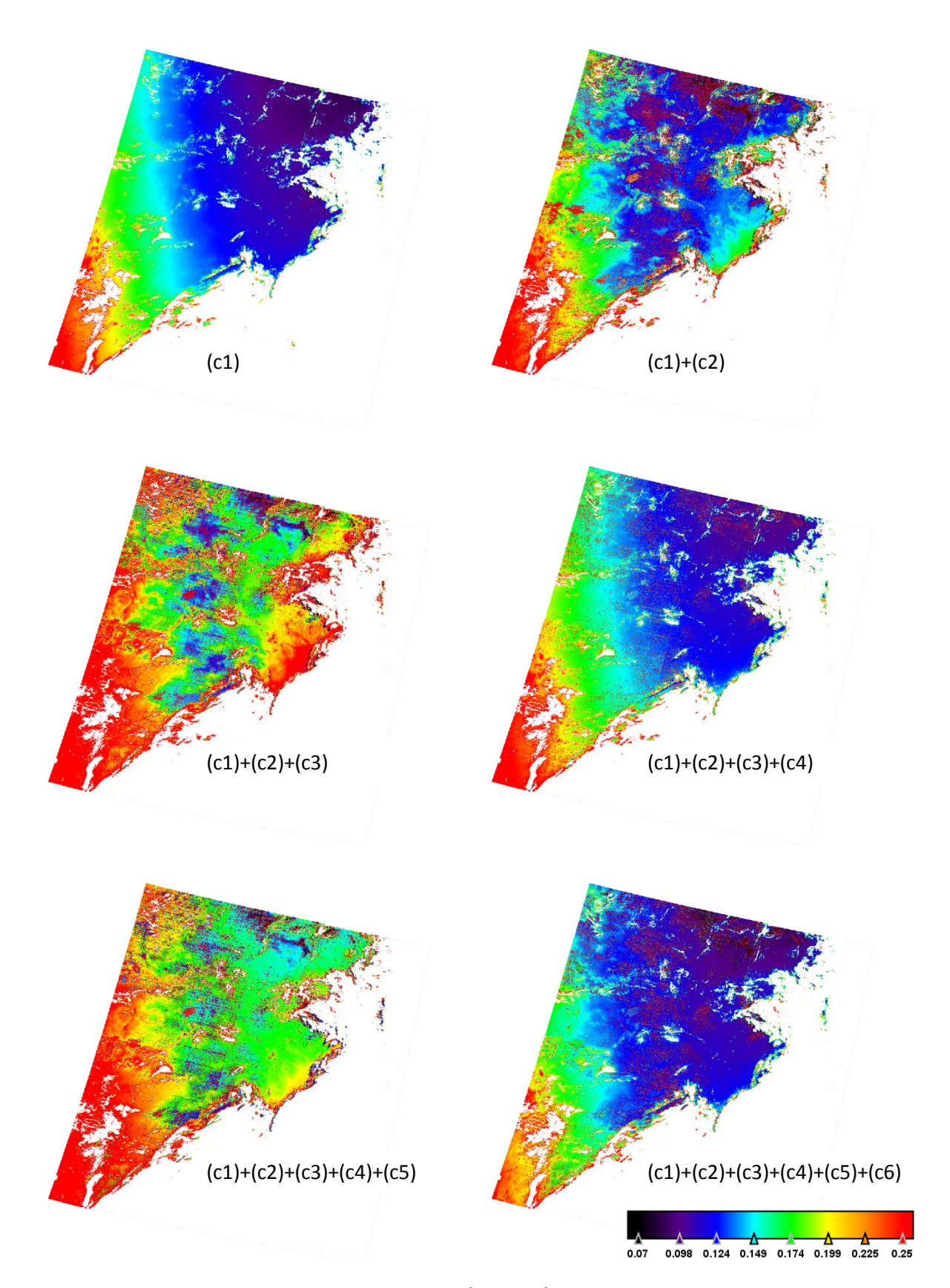


Figure 21: Contributing terms to total uncertainty  $var(\rho_w(412))$ ; terms (c1), (c2), (c3), (c4), (c5) and (c6) refers to equation (32). Scale of variance is multiplied by  $10^6$ 



Pixel-by-pixel uncertainty propagation in OLCI clear water branch

Ref.: S3-L2-SD-01-C01-ACR-TN

Version: 2.0

Date: 28/06/2013

Page: 39

### 7 Assumptions and limitations

- This radiometric uncertainty propagation does not include systematic error model (in either atmospheric or bio-optical modelling), which are to be added for providing a complete product uncertainty.
- The proposed approach needs as input the Level 1 radiometric uncertainty; we have shown that not only the band per band noise (SNR) is required, but also the spectral correlation between bands.
- Uncertainties from upstream steps need to be assessed in order to ingest the most realistic error in the atmospheric correction. In particular, extension to turbid waters needs uncertainty estimates at 779 and 865 nm from the bright pixel atmospheric correction. The same approach is directly applicable to such pre-processing steps when they are written in term of analytical algorithms.

#### Acknowledgement

This work is cofunded by ESA/ARGANS (contract GMES Sentinel-3 products and algorithms definition [21456/08/I-EC]) and CNES (contract n°128146). MERIS data were obtained at ACRI-ST. The ODESA software (<a href="http://earth.eo.esa.int/odesa">http://earth.eo.esa.int/odesa</a>) is developed by ESA and ACRI-ST.



Pixel-by-pixel uncertainty propagation in OLCI clear water branch

Ref.: S3-L2-SD-01-C01-ACR-TN

Version: 2.0

Date: 28/06/2013

Page: 40

#### 8 References

Antoine, D. and Fanton d'Andon, O. (2012) Ocean colour products in Case 1 waters, OLCI Level 2 ATBD, ref. S3-L2-SD-03-C10-LOV-ATBD, Issue 2.3

Antoine, D. and Morel, A. (1998). Relative importance of multiple scattering by air molecules and aerosols in forming the atmospheric path radiance in the visible and near-infrared parts of the spectrum, Applied Optics, 37, 2245-2259.

Antoine, D. and A. Morel (1999). A multiple scattering algorithm for atmospheric correction of remotely-sensed ocean colour (MERIS instrument): principle and implementation for atmospheres carrying various aerosols including absorbing ones, International Journal of Remote Sensing, 20, 1875-1916.

M. J. Behrenfeld, R. O'Malley, D. Siegel, C. McClain, J. Sarmiento, G. Feldman, A. Milligan, P. Falkowski, R. Letelier, E. Boss. (2006) Climate-driven trends in contemporary ocean productivity. Nature 444, 752-755

E. S. Boss and S. Maritorena, Uncertainties in the products of ocean-colour remote sensing, in Remote Sensing of Inherent Optical Properties: Fundamentals, Tests of Algorithms and Applications, Z.-P. Lee, ed. (IOCCG, 2006).

Bourg, L., Delwart, S. (2013). MERIS instrument calibration, in prep.

Cox, C. and W. Munk (1954). Measurement of the Roughness of the Sea Surface from Photographs of the Suns Glitter. J. Opt. Soc. Am. 44, 838 – 850.

Donlon, C., B. Berruti, A Buongiorno, M-H Ferreira, P. Femenias, J. Frerick, P. Goryl, U. Klein, H. Laur, C. Mavrocordatos, J. Nieke, H. Rebhan, B. Seitz, J. Stroede, and R. Sciarra (2012) The Global Monitoring for Environment and Security (GMES) Sentinel-3 Mission, Remote Sensing of the Environment, 120,27-57, http://dx.doi.org/10.1016/j.rse.2011.07.024

M. Doron, M. Babin, A. Mangin, and O. Hembise (2007) Estimation of light penetration, and horizontal and vertical visibility in oceanic and coastal waters from surface reflectance. J. Geophys. Res. 112, C06003.

Fanton d'Andon O.H., D. Antoine, A. Mangin, S. Maritorena, D. Durand, Y. Pradhan, S. Lavender, A. Morel, J. Demaria, G. Barrot (2008) Ocean colour sensors characterisation and expected error estimates of ocean colour merged products from GlobColour, Ocean Optics, Barga.

Fanton d'Andon O.H., A. Mangin, S. Maritorena, S. Lavender, D. Antoine, A. Morel, S. Pinnock, (2009) Exploitation of GlobColour dataset: global characterisation of Chlorophyll, aCDM and bbp uncertainties at pixel level, Ocean Obs 09



Pixel-by-pixel uncertainty propagation in OLCI clear water branch

Ref.: S3-L2-SD-01-C01-ACR-TN

Version: 2.0

Date: 28/06/2013

Page: 41

Fox, N. (2010) A guide to expression of uncertainty of measurements, QA4EO guide ref. QA4EO-QAEO-GEN-DQK-006, GEO, March 2010.

B. A. Franz, S. W. Bailey, P. J. Werdell and Ch. R. McClain (2007) Sensor-independent approach to vicarious calibration of satellite ocean color radiometry, Applied Optics 46, No 22, 5068—5082).

Gohin F., Saulquin B., Oger-Jeanneret H., Lozac' h L., Lampert L., Lefebvre A., Riou P., Bruchon F. (2008). Towards a better assessment of the ecological status of coastal waters using satellite-derived chlorophyll-a concentrations. Remote Sensing of Environment, 112(8), 3329-3340

Gordon, H. R., and M. Wang (1994) Retrieval of water-leaving radiance and aerosol optical thickness over the oceans with Sea-WiFS: a preliminary algorithm. Appl. Opt., 33,443–452

W. W. Gregg (2008) Assimilation of SeaWiFS ocean chlorophyll data into a three-dimensional global ocean model, J. Mar. Syst., vol. 69, no. 3/4, pp. 205–225.

C. Hu, K. L. Carder, and F. E. Muller-Karger. (2011) How precise are SeaWiFS ocean color estimates? Implications of digitization-noise errors. Remote Sens. Environ. 76, 239 – 249.

Hu, C., Feng, L., Lee, Z-P., Davis, C.O., Mannino, A., McClain, C.R., and Franz, B.A. (2012). Dynamic range and sensitivity requirements of satellite ocean color sensors: learning from the past. Applied Optics, 51(25): 6045-6062

JCGM (BIPM, IEC, IFCC, ISO, IUPAC, IUPAP and OIML) (2008) Evaluation of measurement data — Guide to the expression of uncertainty in measurement. JCGM 100:2008. BIPM edition, September 2008.

Lee, Z., Arnone, R., Hu, C., Werdell, J., Lubac, B. (2010). Uncertainties of optical parameters and their propagations in an analytical ocean color inversion algorithm. Appl Opt 49 (3): 369-81

MERIS Quality Working Group (2011) MERIS 3rd data Reprocessing: Software and ADF updates, Report no. A879.NT.008.ACRI-ST, 21091/07/I-OL, available at: http://earth.eo.esa.int/pcs/envisat/meris/documentation/

Lerebourg, C., Mazeran, C., Huot, J-P., Antoine, A. (2011) Vicarious adjustment of the MERIS Ocean Colour Radiometry. MERIS ATBD 2.24, Issue 1.0

Maritorena, S., O. Hembise Fanton d'Andon, A. Mangin & D.A. Siegel (2010). Merged Ocean Color Data Products Using a Bio-Optical Model: Characteristics, Benefits and Issues. Remote Sensing of Environment

Martinez E., D. Antoine, F. D'Ortenzio and B. Gentili (2009). Climate-driven basin-scale decadal oscillations of oceanic phytoplankton, Science, 36, 1253-1256.



Pixel-by-pixel uncertainty propagation in OLCI clear water branch

Ref.: S3-L2-SD-01-C01-ACR-TN

Version: 2.0

Date: 28/06/2013

Page: 42

Mazeran, C., Barker, K., Lerebourg, C., Kent, C., Huot, J-P (2012) MERMAID and ODESA: Complementary Marine Bio-optical Processing and Validation Facilities. Proceedings of the 21st Ocean Optics conference – October 8-12 – Glasgow, Scotland

Mélin, F. (2010) Global distribution of the random uncertainty associated with satellite derived Chla. *IEEE Geosci. Remote Sens. Lett.*, 7, 220-224, 10.1109/LGRS.2009.2031825.

Morel, A., and S. Maritorena (2001). Bio-optical properties of oceanic waters: A reappraisal. Journal of Geophysical research, 106, 7763-7780

Morel, A., Antoine, D. and B. Gentili (2002). Bidirectional reflectance of oceanic waters: Accounting for Raman emission and varying particle phase function, Applied Optics, 41, 6289-6306

Morel, A., Huot, Y., Gentili, B., Werdell, P.J., Hooker, S.B. and B.A. Franz (2007). Examining the consistency of products derived from various ocean color sensors in open ocean (Case 1) waters in the perspective of a multi-sensor approach. Remote Sensing of Environment, 111, 69-88.

Morel, A., Antoine, D. (2011) Pigment index retrieval in Case 1 waters. MERIS ATBD 2.9, Issue 4.3

Moore, G. and Lavender, S. (2011) Case II.S Bright Pixel Atmospheric Correction. MERIS ATBD 2.6, Issue 5.0

Moore, T. S., J. W. Campbell, and M. D. Dowell (2009) A class-based approach to characterizing and mapping the uncertainty of the MODIS ocean chlorophyll product. Remote Sensing of Environment, 113, 2424-2430.

J. Nieke, F. Borde, C. Mavrocordatos, B. Berruti, Y. Delclaud, J.-B. Riti, T. Garnier (2012) The Ocean and Land Colour Imager (OLCI) for the Sentinel 3 GMES Mission: status and first test results, Proc. SPIE 8528, Earth Observing Missions and Sensors: Development, Implementation, and Characterization II, 85280C (November 27, 2012); doi:10.1117/12.977247

Saulquin, B., R. Fablet, A. Mangin, G. Mercier, D. Antoine, and O. Fanton d'Andon, 2013, Detection of linear trends in multisensor time series in the presence of autocorrelated noise: Application to the chlorophyll-a SeaWiFS and MERIS data sets and extrapolation to the incoming Sentinel 3-OLCI mission, submitted to J. Geophys. Res. Oceans.

Triantafyllou, G., Korres, G., Hoteit, I., Petihakis, G., and Banks, A. C. (2007) Assimilation of ocean colour data into a Biogeochemical Flux Model of the Eastern Mediterranean Sea, Ocean Sci., 3, 397-410, doi:10.5194/os-3-397-2007

P. Wang, E. Boss, and C. Roesler (2005) Uncertainties of inherent optical properties obtained from semi-analytical inversions of ocean color. Appl. Opt. 44, 4074 – 4085 (2005).



Pixel-by-pixel uncertainty propagation in OLCI clear water branch

Ref.: S3-L2-SD-01-C01-ACR-TN

Version: 2.0

Date: 28/06/2013

Page: 43

Werdell, P.J. and S.W. Bailey (2005) An improved bio-optical data set for ocean color algorithm development and satellite data product validation. Remote Sensing of Environment, 98, 122-140

Zagolski, F. (2010) Specification of the Scientific Contents of the MERIS Level 1b & 2 Auxiliary Data Products, Parbleu technologie report ref. PO-RS-PAR-GS-0002 3C



Pixel-by-pixel uncertainty propagation in OLCI clear water branch

Ref.: S3-L2-SD-01-C01-ACR-TN

Version: 2.0

Date: 28/06/2013

Page: 44

# Annex A Full derivation of atmospheric correction uncertainty propagation

We here complete the computation of equation (30) ad (31) introduced in section 5.1. As said previously, we can use the approximation

$$\partial(\zeta_{\lambda}(y,z)C_{\Lambda P}+(\lambda,y,z)) \approx C_{\Lambda P}+(\lambda,y,z) \,\partial\zeta_{\lambda}(y,z)$$
 (41)

so that we eventually only need derivatives  $\frac{\partial \zeta_{\lambda}}{\partial y}$ ,  $\frac{\partial \zeta_{\lambda}}{\partial z}$ ,  $\frac{\partial t_{\lambda}}{\partial y}$  and  $\frac{\partial t_{\lambda}}{\partial z}$ .

From equations (22) and (24) we get

$$\frac{\partial \zeta_{\lambda}}{\partial y} = \frac{\zeta_{\lambda}^{ia2}(z) - \zeta_{\lambda}^{ia1}(z)}{\zeta_{779}^{ia2}(z) - \zeta_{779}^{ia1}(z)} \tag{42}$$

and

$$\frac{\partial \zeta_{\lambda}}{\partial z} = \left(\frac{\partial \zeta_{\lambda}^{ia2}}{\partial z} - \frac{\partial \zeta_{\lambda}^{ia1}}{\partial z}\right) mix(y, z) + \frac{\partial \zeta_{\lambda}^{ia1}}{\partial z} + \left(\zeta_{\lambda}^{ia2}(z) - \zeta_{\lambda}^{ia1}(z)\right) \frac{\partial mix}{\partial z}$$
(43)

with

$$\frac{\partial mix}{\partial z} = -\frac{1}{\zeta_{779}^{ia2}(z) - \zeta_{779}^{ia1}(z)} \left( \frac{\partial \zeta_{779}^{ia1}}{\partial z} + mix \left( \frac{\partial \zeta_{779}^{ia2}}{\partial z} - \frac{\partial \zeta_{779}^{ia1}}{\partial z} \right) \right) \tag{44}$$

Hence  $\frac{\partial \zeta_{\lambda}}{\partial z}$  relies on the computation of  $\frac{\partial \zeta_{\lambda}^{ia}}{\partial z}$  for both bracketing models (ia1, ia2). From equations (9) and (10) we have

$$\zeta_{\lambda}^{ia} = \mathcal{P}_{\lambda}^{ia} \left( \tau_{a}^{ia}(\lambda) \right) = \mathcal{P}_{\lambda}^{ia} \left( \tau_{a}^{ia}(865) * c_{\lambda}^{ia} \left( \tau_{a}^{ia}(865) \right) \right) \tag{45}$$

Optical thickeness  $\tau_a^{ia}(865)$  is retrieved by polynomial inversion of  $z=\zeta_{865}*\mathcal{C}_{\Delta P^-}(865)$ :

$$\tau_a^{ia}(865) = \mathcal{P}_{865}^{i^{-1}}(z) \qquad (46)$$

For the derivation of (44), w0e remind the generale rule

$$\left(\mathcal{P}_{865}^{i^{-1}}\right)'(z) = \frac{1}{\mathcal{P}_{865}^{i'}\left(\mathcal{P}_{865}^{i^{-1}}(z)\right)} = \frac{1}{\mathcal{P}_{865}^{i'}\left(\tau_a^{ia}(865)\right)} \tag{47}$$

which gives

$$\frac{\partial \tau_a^{ia}(\lambda)}{\partial z} = \frac{1}{\mathcal{P}_{865}^{ia'}(\tau_a^{ia}(865))} \left( c_{\lambda}^{ia}(\tau_a^{ia}(865)) + \tau_a^{ia}(865) * c_{\lambda}^{ia'}(\tau_a^{ia}(865)) \right)$$
(48)



Pixel-by-pixel uncertainty propagation in OLCI clear water branch

Version: 2.0

Ref.:

Date:

ersion: 2.0

28/06/2013

S3-L2-SD-01-C01-ACR-TN

Page: 45

This equation introduces the derivative  $c_{\lambda}^{ia'}$ ; practically since  $c_{\lambda}^{ia}(\tau)$  comes from a linear interpolation in a Look-up table, the derivative can be computed numerically, by a piecewise constants function. Eventually one has

$$\frac{\partial \zeta_{\lambda}^{ia}}{\partial z} = \mathcal{P}_{\lambda}^{ia'} \left( \tau_{a}^{ia}(\lambda) \right) * \frac{\partial \tau_{a}^{ia}(\lambda)}{\partial z} \tag{49}$$

For the transmittance, one has similarly from equations (23) and (24)

$$\frac{\partial t_{\lambda}}{\partial y} = \frac{\ln t_{\lambda}^{ia2}(z) - \ln t_{\lambda}^{ia1}(z)}{\zeta_{779}^{ia2}(z) - \zeta_{779}^{ia1}(z)} t_{\lambda}$$
 (50)

and

$$\frac{\partial t_{\lambda}}{\partial z} = \left( \left( \frac{1}{t_{\lambda}^{ia2}} \frac{\partial t_{\lambda}^{ia2}}{\partial z} - \frac{1}{t_{\lambda}^{ia1}} \frac{\partial t_{\lambda}^{ia1}}{\partial z} \right) mix(y, z) + \frac{1}{t_{\lambda}^{ia1}} \frac{\partial t_{\lambda}^{ia1}}{\partial z} + \left( \ln t_{\lambda}^{ia2}(z) - \ln t_{\lambda}^{ia1}(z) \right) \frac{\partial mix}{\partial z} \right) t_{\lambda}$$
(51)

Because  $t_{\lambda}^{ia}$  is directly interpolated from Look-up tables indexed by optical thickness, we can either compute  $\frac{\partial t_{\lambda}^{ia}}{\partial z}$  numerically or, as proposed here, consider the approximate analytical expression:

$$\ln t_{\lambda}^{ia} = -\left(\frac{\tau_{R}(\lambda)}{2} + \left(1 - \omega_{\lambda}^{ia} f_{\lambda}^{ia}\right) \tau_{a}^{ia}(\lambda)\right) * M$$
 (52)

where  $\tau_R$  is the Rayleigh optical thickness at actual pressure, M is the air mass fraction of the two-way path M=1/cos( $\theta_{\rm s}$ )+1/cos( $\theta_{\rm v}$ ) ( $\theta_{\rm s}$  and  $\theta_{\rm v}$  being respectively the sun and viewing zenithal angles),  $\omega_{\lambda}^{ia}$  and  $f_{\lambda}^{ia}$  respectively the single scattering albedeo and forward scattering probability of aerosol model ia, which gives

$$\frac{1}{t_{\lambda}^{ia}} \frac{\partial t_{\lambda}^{ia}}{\partial z} = -\left(1 - \omega_{\lambda}^{ia} f_{\lambda}^{ia}\right) * M * \frac{\partial \tau_{a}^{ia}(\lambda)}{\partial z}$$
 (53)

This completes the derivation.

To summarise, the uncertainty computation on water-leaving reflectance can be implemented in the following way:

1. Get from the standard atmospheric correction the bracketing aerosol models (ia1, ia2) and for both of them  $\tau_a^{ia}(865)$ ,  $\tau_a^{ia}(\lambda)$ ,  $\omega_\lambda^{ia}$ ,  $f_\lambda^{ia}$ ,  $\zeta_\lambda^{ia}$ ,  $t_\lambda^{ia}$ , coefficients of  $\mathcal{P}_\lambda^{ia}$  as well as the mixing ratio mix and  $t_\lambda$  and  $\rho_w$  resulting from the mixing

For both models ia1, ia2:

2. Evaluate  $c_{\lambda}^{ia'}$ 



Pixel-by-pixel uncertainty propagation in OLCI clear water branch

Ref.: S3-L2-SD-01-C01-ACR-TN

Version: 2.0

Date: 28/06/2013

Page: 46

3. Evaluate  $\frac{\partial \tau_a^{ia}(\lambda)}{\partial z}$  by equation (48). This needs the derivative of  $\mathcal{P}_{865}^{ia}$  which are directly given by the polynomial coefficients.

- 4. Evaluate  $\frac{\partial \zeta_{\lambda}^{i}}{\partial z}$  by equation (49). Same remark on derivative of  $\mathcal{P}_{\lambda}^{ia}$
- 5. Evaluate  $\frac{1}{t_{\lambda}^{ia}} \frac{\partial t_{\lambda}^{ia}}{\partial z}$  by equation (53) and (48)
- 6. Compute  $\frac{\partial mix}{\partial z}$  by equation (44)
- 7. Compute  $\frac{\partial \zeta_{\lambda}}{\partial y}$  by equation (42) and  $\frac{\partial \zeta_{\lambda}}{\partial z}$  by equation (43)
- 8. Compute  $\frac{\partial t_{\lambda}}{\partial y}$  by equation (50) and  $\frac{\partial t_{\lambda}}{\partial z}$  by equation (51)
- 9. Compute  $\frac{\partial f}{\partial x'}$ ,  $\frac{\partial f}{\partial y}$  and  $\frac{\partial f}{\partial y}$  by equations (29)-(30)-(31)
- 10. Compute  $var(\rho_w(\lambda))$  by equation (25) and known covariance matrix (26). The square root  $\sigma(\rho_w(\lambda))$  can be stored as the final OLCI uncertainty product.
- 11. Compute  $cov(\rho_w(\lambda_1), \rho_w(\lambda_2))$  for all band pairs  $(\lambda_1, \lambda_2)$  in the visible by equation (27)-(28) for further ocean colours product uncertainty propagation

**End Of Document**